Title

Inhibition of Axon Regeneration by Liquid-like TIAR-2 Granules

Journal

Neuron, 104(2)

ISSN

0896-6273

Authors

Andrusiak, Matthew G
Sharifnia, Panid
Lyu, Xiaohui
et al.

Publication Date

2019-10-01

DOI

10.1016/j.neuron.2019.07.004

Peer reviewed

HHS Public Access

Author manuscript

Neuron. Author manuscript; available in PMC 2020 October 23.

Published in final edited form as:

Neuron. 2019 October 23; 104(2): 290–304.e8. doi:10.1016/j.neuron.2019.07.004.

Inhibition of axon regeneration by liquid-like TIAR-2 granules

Matthew G. Andrusiak[1], **Panid Sharifnia**[1,#], **Xiaohui Lyu**[1], **Zhiping Wang**[1,#], **Andrea M. Dickey**[1], **Zilu Wu**[1], **Andrew D. Chisholm**[1], **Yishi Jin**[1,2,*]

[1.] Neurobiology Section, Division of Biological Sciences, University of California, San Diego, La Jolla, CA 92093, USA.

[2.] Lead Contact

Summary

Phase separation into liquid-like compartments is an emerging property of proteins containing prion-like domains (PrLDs), yet the *in vivo* roles of phase separation remain poorly understood. TIA proteins contain a C-terminal PrLD, and mutations in the PrLD are associated with several diseases. Here, we show that the *C. elegans* TIAR-2/TIA protein functions cell-autonomously to inhibit axon regeneration. TIAR-2 undergoes liquid-liquid phase separation *in vitro,* and forms granules with liquid-like properties *in vivo.* Axon injury induces a transient increase in TIAR-2 granule number. The PrLD is necessary and sufficient for granule formation and inhibiting regeneration. Tyrosine residues within the PrLD are important for granule formation and inhibition of regeneration. TIAR-2 is also serine-phosphorylated *in vivo.* Non-phosphorylatable TIAR-2 variants do not form granules and are unable to inhibit axon regeneration. Our data demonstrate an *in vivo* function for phase separated TIAR-2 and identify features critical for its function in axon regeneration.

eTOC Blurb

Andrusiak et al. identify the PrLD containing protein, TIAR-2, as an intrinsic inhibitor of axon regeneration in *C. elegans.* TIAR-2 undergoes liquid-liquid phase separation into granules *in vivo* which is required to inhibit axon regeneration.

Andrusiak et al. identify liquid-like granules of the protein TIAR-2 as inhibitory for axon regeneration. The prion-like domain, and key sequence features within it, are essential for granule formation providing a functional *in vivo* readout for a phase separated compartment.

[*]Correspondence: yijin@ucsd.edu.

[#]Present address: PS –Department of Psychiatry, University of California, San Francisco.

ZW -Institute of Neuroscience, Zhejiang University, Hangzhou, China.

Author Contributions

MGA, PS, ADC, and YJ conceived and designed the study. Experiments were performed by MGA, PS, XL, AMD, and ZW. ZPW generated reagents and protocols for CRISPR/Cas9 mediated single-copy insertion. MGA, PS, XL, ADC and YJ analyzed the data. MGA, ADC and YJ wrote the manuscript.

Declaration of Interests

The authors declare no competing interest.

Graphical Abstract

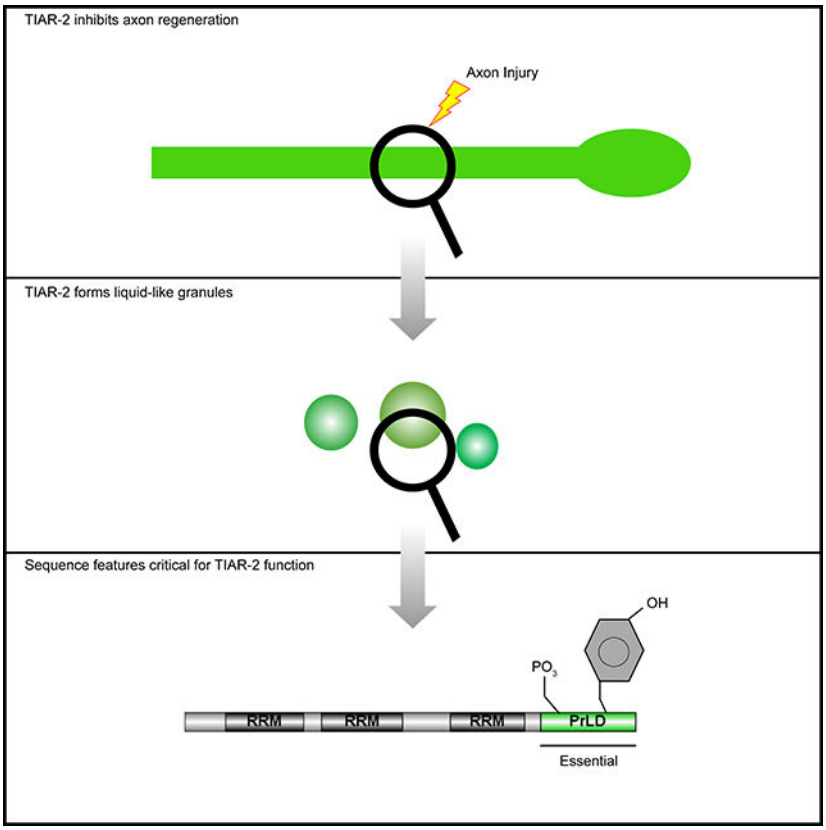

Introduction

The reversible accumulation of RNA-binding proteins into large complexes, termed RNA granules, occurs in normal physiological contexts; however, in many diseases, this accumulation is irreversible (Buchan, 2014; Guzikowski et al., 2019; Van Treeck and Parker, 2019). The accumulation of RNA-binding proteins into granules has been observed following acute insults including stroke and traumatic brain injury (Anderson et al., 2018; Hu et al., 2000; Kahl et al., 2018; Uryu et al., 2007), but it is unknown how this affects neuronal injury responses. An increasing body of evidence has revealed changes in the biophysical properties of granule-forming proteins, such as liquid-liquid and liquid-solid transitions, under normal and pathogenic circumstances (Shin and Brangwynne, 2017). Understanding how changes in biophysical properties, such as liquid-liquid phase separation (LLPS), affect biological function *in vivo* is critical to understanding the biology of normal and diseased cells.

The TIA family of proteins functions in many cell types, and reversibly accumulate into liquid-liquid phase separated granules following stress (Sanchez-Jimenez and Izquierdo, 2015). Humans encode two TIA family members, TIA1 and TIAR, both of which contain three RNA recognition motifs (RRM) and a C-terminal intrinsically disordered prion-like domain (PrLD) (Figure 1A). PrLDs share sequence characteristics reminiscent of

experimentally determined prions, which are self-templating proteins capable of forming protein aggregates (Harrison and Shorter, 2017). Mutations in the PrLD of TIA1 have been linked to diseases (Hackman et al., 2013; Klar et al., 2013; Mackenzie et al., 2017) and were shown to enhance its ability to undergo LLPS (Mackenzie et al., 2017). Though TIA1 deregulation disrupts its granule dynamics, the functional correlates of TIA family proteins in LLPS remain to be determined.

Here, we investigate the role of TIA family proteins in axon regeneration after injury, a process highly dependent on cell intrinsic mechanisms (He and Jin, 2016). We exploit the nematode *C. elegans,* an excellent model for studying the cell biology of axon regeneration *in vivo* (Hammarlund and Jin, 2014; Yanik et al., 2004). Findings on *C. elegans* axon regeneration have highlighted the importance of conserved cell-intrinsic regulators of regrowth such as MAP kinase signaling and microtubule dynamics (Chen et al., 2011; Hammarlund et al., 2009; Kim et al., 2018; Nix et al., 2014; Yan et al., 2009). The *C. elegans* genome encodes two bona fide TIA family proteins, TIAR-1 and TIAR-2. TIAR-1 has been reported to form granules in the germline, and protects germ cells from stress (Huelgas-Morales et al., 2016; Silva-Garcia and Estela Navarro, 2013). TIAR-2 forms granules in the germline in response to stress (Jud et al., 2008) and accumulates in pharyngeal muscle with age (Lechler et al., 2017). The *in vivo* functions and biophysical properties of TIAR-2 in the nervous system have not been previously investigated.

We report that *tiar-2* acts intrinsically to repress the early stages of axon regeneration. TIAR-2 forms liquid-like granules in axons that increase in number following injury, correlating with the early regeneration response. The PrLD of TIAR-2 is necessary and sufficient to inhibit axon regrowth and to form granules. We show that tyrosine residues within the PrLD are critical for both granule formation and inhibition of axon regrowth. Moreover, the PrLD of TIAR-2 is serine phosphorylated *in vivo*, and phospho-mimetic residues retain their ability to form granules and inhibit regeneration, whereas this is lost in phospho-deficient mutants. Together, our data demonstrate that the formation of a liquid-like granule impairs a neuronal injury response.

Results

tiar-2 is an intrinsic inhibitor of the early stages of axon regeneration

We screened for *C. elegans* genes affecting axon regeneration *in vivo* using laser axotomy of PLM mechanosensory axons (Chen et al., 2011; Kim et al., 2018) and identified the TIA family member *tiar-2* as an inhibitor of axon regrowth. In two independent null (*0*) alleles of *tiar-2*, *tm2923* and *ju1401* (Figures 1A and S1A–B), PLM axons developed normal morphology, but showed a significant increase in axon regrowth following injury compared to controls (Figure 1B–C). We also observed increased axon regeneration in the ALM neuron in *tiar-2(0)* animals (Figure S1C). Loss of function in *tiar-1,* or in genes whose orthologs are known to interact with TIA1, showed normal axon regrowth (Table S1), supporting a specific role for *tiar-2* in axon regeneration.

To determine in which cell(s) *tiar-2* functions, we constructed a GFP-TIAR-2 mini-gene translational reporter (Figure S1D) and observed broad expression in many cell types

including mechanosensory neurons (Figure S1D). We next expressed *tiar-2* cDNA as a genomically integrated single-copy (Si) transgene in mechanosensory neurons (P_{mec-4}-*GFP-TIAR-2*[*juSi306*]*),* or muscles (P_{myo-3}-*GFP-TIAR-2*[juSi324]). We found that expression of *tiar-2* in mechanosensory neurons, but not in muscles, restored the increased regrowth of *tiar-2(0)* mutants to control levels (Figure 1B–C), supporting a cell-autonomous role for *tiar-2* in axon regeneration. Moreover, expression of human TIA1 (P_{mec-4}-*GFP-hTIA1*[*juSi340*]*)* in mechanosensory neurons restored the increased axon regrowth in *tiar-2(0)* to control level (Figure 1B–C), supporting that TIAR-2 and human TIA1 have conserved function.

In *C. elegans* PLM, severed axons begin regrowth around 3–6 hours post-injury, followed by sustained axon extension over several days (Chen et al., 2011; Ghosh-Roy et al., 2012). The axon regrowth rate in *tiar-2(0)* was significantly higher from 0 – 6 h (2.15 fold to control) than in later time periods (Figure 1D–E). PLM axons in *tiar-2(0)* displayed more filopodia at 3 h post-injury (Figure 1F–G) and more growth cones at 6 h post-injury, compared to control (Figure 1H–I). These data show that *tiar-2* represses the early phase of the regenerative response to injury.

TIAR-2 forms granules *in vivo* and overexpression of TIAR-2 inhibits axon regeneration

We next examined the subcellular localization of GFP-TIAR-2. In mechanosensory neurons, GFP-TIAR-2 expressed from single-copy [*juSi306*] and multi-copy [*juIs542*] transgenes was present throughout the cell body and axons, appearing as either diffuse or in granules (Figures 2A, S3A). mKate2-TIAR-2 displayed a similar granular pattern (Figure S2B), indicating that granular localization was independent of the fluorescent protein tag. TIAR-2 granules were found at variable positions along the axon (Figure 2A). Mammalian TIA1 shuttles between cytoplasm and nucleus under heat stress (Zhang et al., 2005). We subjected animals expressing P_{mec-4}-GFP-TIAR-2[*juSi306*] to heat shock and observed that GFP-TIAR-2 translocated from the nucleus to cytoplasmic granules (Figure S2C–E). These data support a conserved ability of TIA proteins to form granules in response to stress. *tiar-2* transcript levels correlate with transgene copy number (Figure S2A). As the expression increased, we observed a graded increase in the percentage of PLM axons with GFP-TIAR-2 granules (Figure 2A), which correlated with an increased inhibition of axon regrowth (Figure 2B), suggesting the precise levels of TIAR-2 affect axon regeneration.

TIAR-1 does not form granules in neurons and cannot replace TIAR-2 in axon regeneration

C. elegans TIAR-1 is closely related to TIA1 and to TIAR-2 (Figure S2F), and can form granules in the germline in response to stress (Huelgas-Morales et al., 2016). As loss of *tiar-1* did not affect axon regrowth (Table S1, Figure 2D), we investigated the basis of the functional difference of TIAR-1 and TIAR-2. A knock-was reporter for TIAR-1(TIAR-1-GFP[*tn1545*]) is expressed in mechanosensory neurons (Figure S2G). When specifically driven under the control of a mechanosensory neuronal promoter, GFP-TIAR-1 was diffuse, regardless of expression level (Figure 2C). Moreover, TIAR-1 expression in mechanosensory neurons of *tiar-2(0)* animals did not restore axon regrowth to control level (Figure 2D). This analysis suggests that the ability to form granules likely contributes to the different effects of TIAR-1 and TIAR-2 on PLM axon regeneration.

TIAR-2 granules in neurons are likely heterogenous

To characterize the composition of TIAR-2 granules in PLM neurons, we performed colocalization analysis of several proteins whose orthologs are either known to interact with TIA1 or are core components of various types of RNA granules (Buchan and Parker, 2009). To interpret colocalization fractions we used the colocalization of mKate-2-TIAR-2 (P_{mec-4}-*mKate-2TIAR-2* [*juEx8007/juEx8008*]) with GFP-TIAR-2[*juIs542*]) as a positive control for colocalization, and chose the colocalization of synaptic vesicles (P_{mec-7}-*GFP-RAB-3*[*jsIs821*]) with mitochondria (P_{mec-7}-*tagRFP-COX8A*[*jsIs1073*]) as a negative control (Figures 3A, C, D, F, K, L and S3E–G).

G3BP proteins are core components of stress granules (Tourriere et al., 2003; Zhang et al., 2019) and limit regrowth of peripheral nerves (Sahoo et al., 2018). A GFP knock-in reporter for the *C. elegans* G3BP ortholog GTBP-1-GFP[*ax2053*] was expressed in the cytoplasm of nearly all cells, precluding visualization of individual axons (Figure 3B). In the PLM cell body, mKate2-TIAR-2 partially but significantly colocalized with GTBP-1-GFP granules (Figure 3B, D). We tested the dependency of TIAR-2 granule formation on GTBP-1 by analyzing GFP-TIAR-2[*juSi542*] in *gtbp-1(0)* and observed no detectable difference in granule pattern or penetrance from that of control (Figure 3E). Moreover, *gtbp-1(0)* mutants displayed normal axon regeneration (Table S1). These data suggest that, although GTBP-1 and TIAR-2 partly colocalize, they likely function independently in axon regrowth.

The RNA binding protein Staufen1 is recruited to stress granules and affects their assembly (Thomas et al., 2009). We expressed *C. elegans* STAU-1 in mechanosensory neurons (P_{mec-4}-*mKate2-STAU-1*[*juSi386*]) and observed discrete granules restricted to the cell body, in a pattern distinct from that of GTBP-1 or TIAR-2. GFP-TIAR-2[*juIs542*] showed significant colocalization with STAU-1 granules (Figure S3B, G), yet loss of *stau-1* did not affect GFP-TIAR-2[*juSi542*] granule formation (Figure S3H) and had no effect on axon regrowth (Table S1). This analysis indicates that TIAR-2 granules can form independently of STAU-1.

mRNA Decapping enzymes, DCP/DCAPs, are processing body components (Franks and Lykke-Andersen, 2008; Guzikowski et al., 2019). Expression of the *C. elegans* DCP1A homolog (P_{dcap-1}-*DCAP-1-dsRed*[*bpIs37*]) was limited to discrete granules within the PLM cell body where it did not colocalize with GFP-TIAR-2[*juIs542*] (Figure S3C, G). We also examined AIN-1, the *C. elegans* ortholog of GW182, which is primarily associated with the miRNA-induced silencing complex (miRISC) and processing bodies (Ding et al., 2005; Eystathioy et al., 2003). In the axon and cell body, mKate2-AIN-1 (P_{mec-4}-*mKate2-AIN-1*[*juEx7947/juEx7948*]) granules showed minimal colocalization with GFP-TIAR-2[*juIs542*] (Figure 3G, L, S3D and G). These data suggest that GFP-TIAR-2 granules in neurons are heterogenous, with some fractions that may correspond to classically defined stress granules.

We also analyzed the colocalization of TIAR-2 granules with other axonal components, including synaptic vesicles, active zone proteins, and mitochondria. GFP-TIAR-2[*juIs542*] did not exhibit significant colocalization with either a synaptic vesicle marker (P_{mec-7}-*tagRFP-RAB-3*[*jsIs1263*]) or a presynaptic active zone marker (P_{mec-7}-*tag-RFP-*

ELKS[*jsIs1075*]), and also did not overlap with mitochondria ($P_{mec\text{-}7}$-*tagRFP-COX8A[jsIs1073])* (Figure 3F–L). Therefore, axonal TIAR-2 granules are distinct from mitochondria and synaptic compartments.

TIAR- 2 undergoes liquid-liquid phase separation *in vitro*

Many PrLD containing proteins can form phase separated liquid-like compartments (Chuang et al., 2018). Liquid-liquid phase separation (LLPS) is governed by multivalent interactions that are facilitated by the lack of structural rigidity of PrLDs (Shin and Brangwynne, 2017). We tested whether TIAR-2 could form liquid-like droplets following established protocols (Alberti et al., 2018; Lin et al., 2015). Both GFP-TIAR-2 and TIAR-2 formed phase-separated droplets (Figure 4A). TIAR-2 droplets were able to fuse and increased in size (Figure 4B, Video S1), a hallmark of LLPS. Moreover, GFP-TIAR-2 droplets exhibited rapid recovery following photobleaching (Figure 4C), a characteristic of the highly mobile liquid-like state. Further, we isolated GFP-TIAR-2[*juSi542*] from *C. elegans* mechanosensory neurons and observed that these granules displayed fusion and dripping-like deformation (Video S2). Thus, TIAR-2 exhibits many features associated with LLPS *in vitro,* similar to TIA1 (Mackenzie et al., 2017)

Neuronal TIAR-2 granules show liquid-like features *in vivo*

We addressed whether axonal TIAR-2 granules were in a liquid-like state by characterizing their dynamics in PLM neurons. Three parameters can be assessed to determine liquid-like compartments in an axon *in vivo*: fusion, circularity, and rapid content rearrangement (Gasset-Rosa et al., 2019; Gopal et al., 2017; Tinevez et al., 2017). GFP-TIAR-2 granules displayed short-range oscillatory movement, with minimal overall displacement (Figures 4F, S4B). GFP-TIAR-2[*juIs542*] granules showed fusion (Figures 4E, G and Video S3, S9) and were roughly spherical (Figure 4H), consistent with a liquid-state. The observed properties of GFP-TIAR-2 granules were distinct from those of markers for membrane-bound structures (Figure S4D–G). Synaptic vesicles[*jsIs821*] exhibited long-range movement, consistent with microtubule-based transport, whereas mitochondria[*jsIs1073*] were stationary over the same period (Figure S4E, Video S3–S5). GFP-RAB-3 puncta, but not tagRFP-COX8A, coalesced (Figure S4F, Video S3–S5), reflecting synaptic vesicle clustering (Milovanovic et al., 2018). Similarly, GFP-RAB-3 puncta were largely circular, whereas mitochondria deviated significantly from circularity (Figure S4G). The small size and rapid movement of GFP-TIAR-2 granules (Figure 4D–E) precluded photobleaching experiments to assess content rearrangement *in vivo*. Nonetheless, these data show that TIAR-2 granules *in vivo* display liquid-like features distinct from membrane-bound components.

Axon injury increases the number of TIAR-2 granules and alters their dynamics

We next addressed whether axon injury alters TIAR-2 subcellular localization. We imaged GFP-TIAR-2 before and after axotomy in animals expressing multi-copy or single-copy transgenes, to capture the dynamics while balancing detection limitations due to expression levels from each transgene. PLM axons expressing high-copy GFP-TIAR-2 [*juIs542*] contained granules prior to injury (Figures S4A and Table S2). Within 5 minutes of axon injury, TIAR-2 granule number increased, remaining elevated for 60 minutes and returning to baseline levels by 180 minutes post-injury (Figure S4A). As a control, we analyzed a

high-copy GFP ($P_{mec\text{-}4}$-*GFP*[*zdIs5*]) expressing strain and did not observe any increase in granule number following injury (Figure S4A). In animals expressing a single-copy GFP-TIAR-2[*juSi306*] transgene we did not visually detect granules prior to injury (Figure 4D). We thus adopted a quantitation method that is used to detect other subcellular structures including synapses and liquid-like granules (Bracha et al., 2018; Zhou et al., 2017). We observed a significant increase in TIAR-2 granule number 15 min post-injury (Figure 4D). GFP ($P_{mec\text{-}4}$-*GFP*[*juSi10*]) did not show any changes in granule number, when subjected to the same injury paradigm (Figure 4D). Moreover, we analyzed the dynamics of GFP-TIAR-2[*juIs542*] granules by live imaging, and found that immediately after injury granules became less motile, underwent fewer fusion events, and were less circular than prior to injury (Figure 4E–H and Video S3), suggesting that axon injury can modulate the properties of TIAR-2 granules. Together, these data show that the time course of the changes in GFP-TIAR-2 granules correlates with TIAR-2's ability to inhibit axon regeneration.

The PrLD of TIAR-2 is necessary and sufficient for its function in axon regeneration and granule formation

To determine the roles of TIAR-2 domains in axon regeneration, we generated GFP-TIAR-2 variants in *tiar-2(0)* animals (Figure 5A). All constructs were single-copy insertions under the control of a mechanosensory neuron promoter into the same genomic locus, and none caused defects in axon development (Figure S6). We tested the ability of TIAR-2 variants to restore control level regeneration in *tiar-2(0)* animals. TIAR-2 lacking all three RRM domains ($P_{mec\text{-}4}$-*GFP-TIAR-2(*ΔRRM1–3*)*[*juSi307*]) restored *tiar-2(0)* mutants to control [*zdIs5*] levels of regeneration, comparable to full-length TIAR-2 (Figure 5A). Conversely, TIAR-2 lacking either the entire PrLD ($P_{mec\text{-}4}$-*GFP-TIAR-2(*ΔPrLD*)*[*juSi332*]), or with a truncated PrLD ($P_{mec\text{-}4}$-*GFPTIAR-2(*ΔGlyRich*)*[*juSi330*]), did not affect axon regrowth (Figure 5A). Thus, the PrLD of TIAR-2 is necessary and sufficient to repress axon regrowth.

We then tested the ability of GFP-TIAR-2 variants to form granules when expressed from high-copy number transgenes. TIAR-2 lacking all three RRM domains ($P_{mec\text{-}4}$-*GFP-TIAR-2(*ΔRRM1–3*)*[*juEx7864/juEx7865*]) formed granules (Figure 5B). Conversely, deletion of the PrLD ($P_{mec\text{-}4}$-*GFP-TIAR-2(*ΔPrLD*)*[*juEx7860/juEx7861*]) or removal of part of the PrLD ($P_{mec\text{-}4}$-*GFP-TIAR-2(*ΔGlyRich*)*[*juEx7862/juEx7863*]*) significantly reduced granule formation (Figure 5B). In addition, axonal granules formed by expression of the PrLD ($P_{mec\text{-}4}$-*GFP-TIAR-2(*ΔRRM1–3*)*[*juEx7864/juEx7865*]) of TIAR-2 displayed liquid-like features such as fusion and near circularity (Figure 5C–E, Video S6), similar to full-length TIAR-2. This analysis supports the conclusion that the PrLD is necessary and sufficient for TIAR-2's ability to form liquid-like granules and to inhibit regeneration.

Tyrosine residues in the PrLD of TIAR-2 promote granule formation and activity in axon regeneration

Phase separation is known to depend on interactions involving aromatic amino acids, including π-π and cation-π interactions. We focused on tyrosine residues due to their key roles in mediating phase separation (Lin et al., 2017; Vernon et al., 2018; Wang et al., 2018b). We asked whether TIAR-2 was tyrosine phosphorylated *in vivo* and did not detect this modification of GFP-TIAR-2[*juSi306*] using immunoprecipitation followed by western

blot, in contrast to a positive control, VAB-1-GFP[*juIs24*] (Wang et al., 1999) (Figure 6A). The PrLD of TIAR-2 has nine tyrosine residues (Figure S5A). We created variants in which tyrosine residues were mutated to glycine, designated as 9YG, 6YG or 3YG. Additionally, we created variants in which glycine residues were mutated to tyrosine (7GY, 5GY, 3GY) (Figure 6B, S5A), increasing the total tyrosine content in the PrLD to 16, 14, and 12, respectively. It is widely known that protein concentration alone can affect propensity to form phase separated structures (Alberti et al., 2019). To minimize this caveat, we expressed all variants as single-copy transgenes to ensure consistent expression. We examined their ability to restore control level regeneration in *tiar-2(0)* animals. Substitution of tyrosine residues in the PrLD completely abolished activity independent of the number of tyrosine altered (Figure 6C). The substitution of tyrosine at glycine residues did not further enhance TIAR-2 activity beyond that of wild-type (Figure 6C).

We next determined whether manipulation of tyrosine residues impacted granule formation in PLM axons. Substituting tyrosine residues for glycine in any of the three variants significantly decreased the granule-forming capacity of TIAR-2 (Figure 6D). The addition of tyrosine at glycine residues did not enhance granule-forming ability beyond that of wild-type TIAR-2 (Figure 6D). Moreover, granules formed by a mutant PrLD in which three glycines were converted to tyrosine ($P_{mec\text{-}4}$-*GFP-TIAR-2(3GY)*[*juSi381*]) still exhibited the liquid-like features of fusion and near circularity (Figure 6E–G, Video S7). We then asked whether manipulation of tyrosine residues within the PrLD affected GFP-TIAR-2's ability to respond to injury. We found that GFP-TIAR-2(3GY)[*juSi381*] displayed increased granule formation, whereas GFP-TIAR-2(3YG)[*juSi385*] showed no significant variation in axonal GFP signal 15 min following injury (Figure 6H). These data highlight the importance of tyrosine residues in the formation of phase-separated TIAR-2 granules and inhibition of axon regeneration.

Serine residues in the PrLD of TIAR-2 regulate granule formation and activity in axon regeneration

Phosphorylation of PrLD proteins influences their biophysical properties (Hofweber and Dormann, 2018). We next asked whether TIAR-2 may be regulated by serine phosphorylation, as the PrLD contains ten serine residues (Figures 7B, S5B). By western blot analysis following immunoprecipitation, we found that full length GFP-TIAR-2[*juSi306*] and GFP-TIAR-2(ΔRRM1–3)[*juSi307*] expressed in mechanosensory neurons were both serine phosphorylated (Figure 7A). Variants of GFP-TIAR-2 (described below) with all serines in the PrLD mutated to alanine ($P_{mec\text{-}4}$-*GFP-TIAR-2(10SA)*[*juSi376*] or two serines ($P_{mec\text{-}4}$-*GFP-TIAR-2(2SA)*[*juSi374*]*)* displayed significantly diminished phosphorylation (Figure 7A).

To explore the functional relevance of serine phosphorylation on TIAR-2 granule formation, we generated phospho-mimetic (S>E) and deficient (S>A) variants within the PrLD (Figures 7B, S5B). This strategy has been widely employed to assess the role of phosphorylatable residues on protein assemblies (Larson et al., 2017; Monahan et al., 2017; Wang et al., 2018a), with the caveat that such mutations affect protein charge distribution irrespective of phosphorylation. We designed phospho-deficient and phospho-mimetic constructs

containing mutations in all ten serine residues (10SA and 10SE), the subset of eight serines predicted to be phosphorylated by NetPhos3.1 (8SA and 8SE), and the two serines with the highest confidence predictions (2SA, S338A/S369A and 2SE, S338E/S369E) (Figure 7B, S5B). In a *tiar-2(0)* background all phospho-mimetic GFP-TIAR-2 (S>E) constructs tested were sufficient to restore regrowth to control levels (*juSi375, juSi378, juSi379*) (Figure 7C) and formed granules ([*juEx7972/juEx7973*], [*juEx7988/juEx7989*], [*juEx7990/juEx7991*]) (Figure 7D). Axonal granules formed by GFP-TIAR-2(2SE)[*juEx7990/juEx7991*] displayed liquid-like features (Figure 7E–G, Video S8). In contrast, mutations of the same residues across all three ranges to alanine (10SA, 8SA, 2SA) blocked the ability to restore axon regrowth to control levels (*juSi376, juSi377, juSi374*) (Figure 7C), and diminished granule formation ([*juEx7974/7975*], [*juEx7984/juEx7985*], [*juEx7986/juEx7987*]) (Figure 7D).

Finally, we asked whether serine mutations affected the capacity of TIAR-2 granules to respond to injury. We performed axotomy on GFP-TIAR-2 variants in which two serines were mutated to either glutamic acid (2SE)[*juSi379*] or alanine (2SA)[*juSi374*]. The GFP-TIAR-2(2SE) variant was competent to form granules following injury, whereas GFP-TIAR-2(2SA) inhibited this property (Figure 7H). These data support the contribution of PrLD serine residues to inhibition of axon regeneration and granule formation.

Discussion

TIA proteins have been studied in multiple cellular processes including stress granule formation, RNA splicing (Damgaard and Lykke-Andersen, 2011; Del Gatto-Konczak et al., 2000; Kedersha et al., 1999), and diseases, such as ALS and WDM (Hackman et al., 2013; Klar et al., 2013; Mackenzie et al., 2017). Here, our study reveals that a *C. elegans* TIA family member, TIAR-2, acts as an intrinsic inhibitor of axon regeneration following injury. We show that TIAR-2 undergoes LLPS *in vitro* and forms liquid-like granules *in vivo* which increase following injury. TIAR-2's ability to form granules and repress axon regrowth are dependent on its PrLD, suggesting that granule formation is closely related to its *in vivo* function. Our structure-function analyses reveal that tyrosine and serine residues in the PrLD are both critical for granule formation and axon regeneration. With the emerging importance of liquid-like states in many cellular processes (Shin and Brangwynne, 2017), our data show how acute injury alters the properties of axonal liquid-like granules and how such granules may regulate the response to injury.

Changes in the biophysical properties of a protein, such as LLPS occur in diverse cellular conditions (Boeynaems et al., 2018) and can be modulated by post-translational modifications, RNA, ATP, and ions (Boeynaems et al., 2017a; Fay et al., 2017; Monahan et al., 2017; Patel et al., 2017; Rayman et al., 2018). Axon injury results in a disruption in membrane integrity, leading to imbalances in intracellular ion levels (Bradke et al., 2012; He and Jin, 2016). Zn^{2+} chelation following optic nerve injury improves neuronal survival and regeneration (Li et al., 2017; Trakhtenberg et al., 2018). Interestingly, the LLPS capacity of TIA1 is promoted by increasing levels of intracellular Zn^{2+} (Rayman et al., 2018). ATP, independent of its role in phosphate transfer, can impair phase separation of FUS (Patel et al., 2017). It is conceivable that local ATP concentrations fluctuate dramatically following axon injury, due to dilution of the cytoplasm by extracellular flux and mitochondrial

dysfunction, resulting in local deficits that may create an environment permissive to phase separation. This is supported by evidence that local injection of ATP supports regeneration of spinal sensory axons (Wu et al., 2018), increases in mitochondrial density correlate with improved regeneration (Cartoni et al., 2017; Han et al., 2016) and several mitochondrial genes regulate regeneration (Cartoni et al., 2016; Knowlton et al., 2017; Zhou et al., 2016). We speculate that injury triggers changes in the axonal microenvironment, such as increased Zn^{2+}, or reduced ATP, that alter the biophysical properties of TIAR-2 granules into a regeneration-inhibitory state.

In proteins such as FUS family members, tyrosine residues promote phase separation due to their ability to form weak molecular interactions via their aromatic ring with other aromatic rings (π-π) or cationic interactions (cation-π) (Lin et al., 2017; Qamar et al., 2018; Vernon et al., 2018; Wang et al., 2018b). Our data expands upon these *in vitro* studies and have identified sequence features that drive TIAR-2 phase separation and affect its ability to inhibit axon regeneration, linking phase separation to *in vivo* function. We show that TIAR-2 is not tyrosine phosphorylated, thus allowing us to uncouple this from other tyrosine effects such as π-interactions. We find that tyrosine residues play an important role in the regulation of TIAR-2 granule formation and during axon regrowth. However, it is interesting to note that simply increasing the number of tyrosines in the PrLD domain does not alter TIAR-2's function, suggesting specificity in their role in TIAR-2 function. We further find that TIAR-2 is serine phosphorylated, as reported for TIA1 (Huang et al., 2014). Phosphorylation can both positively and negatively regulate LLPS of a number of proteins (Hofweber and Dormann, 2018). Though mutation of serine residues in TIA1 has not been reported in cases of WDM or ALS, the mutation of residues in their vicinity may impact kinase/phosphatase recognition resulting in granule deregulation. An understanding of the specific signaling cascades involved in the phosphorylation and dephosphorylation of TIA family proteins will inform on granule dynamics and their association with disease.

Examination of the acute effects of axon and brain damage on proteins such as the TIA family and other granule-associated proteins is of great importance, given the emerging evidence for their deregulation in these conditions (Anderson et al., 2018; Hu et al., 2000; Kahl et al., 2018; Uryu et al., 2007). We have shown that liquid-like granules of TIAR-2 are altered by injury and inhibit the regenerative response. Though many cellular processes are now being associated with liquid-like states, we are just beginning to appreciate how biophysical properties relate to physiological outcomes and how they may be altered in pathological conditions (Shin and Brangwynne, 2017). Our data demonstrate that sequence features that drive liquid-phase separation have a direct impact on protein function following axon injury. The identification of axon injury as modulating granule formation has implications for our understanding of the pathophysiology of acute events such as stroke and traumatic brain injury and their relationship to chronic neurodegenerative disorders.

Star * Methods

Lead Contact and Material Availability

Further information and requests for resources and reagents should be directed to and will be fulfilled by the Lead Contact, Yishi Jin (yijin@ucsd.edu).

Experimental Model and Subject Details

The nematode *Caenorhabditis elegans* was used as the experimental model for this study. All experiments were performed with hermaphrodite animals; males were used only for crosses. Strains were maintained at 20˚C as described in (Brenner, 1974). New strains were constructed using standard procedures and all genotypes confirmed by PCR or sequencing. Extrachromosomal array transgenic lines were generated as described (Mello et al., 1991), and at least two independent lines were analyzed per expression construct. $P_{mec\text{-}4}$-GFP-TIAR-2 [*juIs542*] was integrated from *juEx6526* following UV/TMP mutagenesis. All experiments were performed on L4 animals unless stated otherwise. All experiments were performed on multiple different days.

METHOD DETAILS

CRISPR/Cas9 Genome Editing—*tiar-2(ju1401)* was generated using the *dpy-10* co-CRISPR method (Paix et al., 2015). Briefly, crRNAs for *tiar-2* (Integrated DNA Technologies) were designed towards two sites approximately 500 bp apart and were co-injected with purified Cas9 (28 μM, Macrolabs, University of California, Berkeley) plus *dpy-10* crRNA. F1 worms were initially selected for the Dpy phenotype and then genotyped for *tiar-2* genomic lesions. Putative genome-edited animals were outcrossed to N2 to remove any *dpy-10* mutations. Sanger sequencing was performed to determine the deletion breakpoints in *ju1401*.

Single-copy insertion transgenes were generated at *cxTi10882,* a region of Chromosome IV devoid of known protein coding genes (Frokjaer-Jensen et al., 2008), using a modified protocol. In brief, we designed an sgRNA targeting *cxTi10882* and injected N2 hermaphrodites with three plasmids, one expressing Hyg^R+GFP-cDNA flanked by homology arms (see Key Resources Table for *juSi* plasmids), pCZGY2750 expressing Cas9+sgRNA (*cxTi10882*), and pCJF90 $P_{myo\text{-}2}$-mCherry, a gift from Erik Jorgensen, as a co-injection marker. Animals containing genomic insertion were selected based upon resistance to hygromycin (Hyg^R) and the absence of co-injection markers. Insertion lines were verified by PCR genotyping and sequencing.

Laser Axotomy—L4 stage hermaphrodites were immobilized with 0.05% levamisole in M9 buffer and mounted on 2% agar pads. Axons were severed using a femtosecond laser as described in (Wu et al., 2007). Animals were recovered and cultured on normal NGM plates at 20C and imaged 24 h later using 63X magnification on a Zeiss LSM 510 or 710 confocal microscope. Regrowth length was measured as previously described (Chen et al., 2011; Wu et al., 2007). To account for day-to-day variability in the regeneration response, regrowth data from mutant animals were normalized to control animals axotomized on the same day. Non-normalized raw values are presented in Table S2.

Molecular Biology—*tiar-2* cDNA was cloned from a mixed-stage cDNA library made from wild-type N2 animals. hTIA1 cDNA was cloned from total RNA isolated from human embryonic kidney cells. cDNA was T/A cloned into the pCR8 vector (Life Technologies), and then subsequently cloned into the destination vector $P_{mec\text{-}4}$-GFP-*let-858*(3’ UTR) (pCZGY603). Variants of GFP-TIAR-2 were made using Gibson cloning (New England

Biolabs). Tyrosine and serine variants were created using gBlocks Gene Fragments (Integrated DNA Technologies), designed with the desired amino acid substitutions for *C. elegans* preferred codons.

For qRT-PCR analysis, total RNA was isolated from mixed-staged animals using TRIzol solution (Thermo Fisher), followed by treatment with TurboDNase (Thermo Fisher) and purified with an additional TRIzol extraction. 3 μg of RNA was reverse transcribed into cDNA using an oligo-dT primer and the SuperScript III® First Strand Synthesis System (Life Technologies). Quantitative PCR was performed using iQ SYBR Green Supermix (Bio-Rad) on a C1000 Thermal Cycler with a CFX96 Real-time system (Bio-Rad).

TIAR-2 Granule Quantification—Granule penetrance was scored in live animals using a Zeiss Axioplan 2 microscope equipped with Chroma HQ filters at 63X magnification. L4 stage worms were immobilized with 0.1% levamisole and granules were scored as either present or absent in both PLM neurons. Granules were visualized as both defined foci within the cell body/axon, as well as loss of GFP signal from the nucleus.

GFP-TIAR-2 granule number in PLM axons was analyzed from the tip of the severed proximal axon to the cell body (~30 μm) immediately before and after laser axotomy in identical regions. In detail, PLM axons of immobilized L4 animals were imaged on a Zeiss 710 confocal microscope using a 63X objective with ZEN software (Zeiss) and analyzed using the FIJI package on ImageJ (Schindelin et al., 2012). GFP-TIAR-2 granules in high-copy strains were visibly detectable, and were quantified following the procedure outlined in (Rieckher and Tavernarakis, 2017). In brief, confocal images were equally thresholded, and granules were identified using the 'Analyze Particles' function of FIJI. All values were normalized to granules present pre-axotomy (as time zero); raw granule counts are available in Table S2. GFP-TIAR-2 granules in single-copy strains was defined as a region of the axon that spanned a minimum of two sequential values (~0.15μm), with an intensity value at least one standard deviation ($StDev^{T=0}$) above the average value using the "Plot Profile" function on FIJI (Bracha et al., 2018). To account for variation in the baseline granule number, all animals were normalized to the number of granules present immediately prior to axon injury (Granules at T_{15min}/Granules at T_0). Raw granule values are available in Table S2.

To visualize GFP-TIAR-2 dynamics in live animals immediately following injury, animals were imaged using a Yokogawa CSU-XA1 spinning disc confocal head and a Photometrics Cascade II EMCCD camera (1024 × 1024) controlled by μManager (www.micro-manager.org) with 200 images collected with a 330 ms exposure time. Granule displacement and fission/fusion in PLM axons were analyzed using the TrackMate plugin for FIJI (Schindelin et al., 2012; Tinevez et al., 2017). In brief, GFP-TIAR-2 granules were tracked using the DoG detector, using an estimated blob diameter of 1 μm, linear assignment problems (LAP) tracker and maximum linking distance of 0.5 μm. For analysis of granules following axotomy, frames containing femtosecond laser firing, as well as a single frame before and after firing of the laser were removed. Analysis was performed from the region of axotomy to the beginning of the cell body. Fission and fusion events were normalized to axon length and duration of imaging. Kymographs were created using the MultiKymograph plugin on the FIJI package of ImageJ.

Colocalization analysis—Live L4 stage hermaphrodite animals co-expressing desired pairs of proteins tagged with GFP, mKate2 or tagRFP were immobilized with 0.1% levamisole in M9 buffer and mounted on 2% agar pads. Confocal images were taken using 63X magnification on a Zeiss LSM 710 microscope using a pinhole size adjusted to 1 airy unit. The PLM axon or cell body were set as region of interest and analyzed using 'Coloc2' plugin on FIJI (https://imagej.net/Coloc_2)(Glebov et al., 2016; Rieckher et al., 2018). For axons, maximum intensity z-projections were analyzed, as they project in multiple planes, whereas cell body quantification was performed on a single section. The average Mander's Correlation value for each animal was calculated based on 2–3 10–20 μm regions for axons and two regions for the cell body. N values noted represent the number of animals, not regions. For all extrachromosomal alleles, a minimum of 2 independent transgenic lines were analyzed.

In vitro analysis of TIAR-2 droplet formation—cDNA of *tiar-2* was sub-cloned using Gibson assembly into pET15-MHL, a gift from Cheryl Arrowsmith (Addgene plasmid #26092). Proteins were purified from Rosetta cells (Novagen) as described (Kato et al., 2012) with the following modifications. Purified elutes were concentrated and buffer exchanged into Droplet Buffer (50 mM Tris, 150 mM NaCl pH 7.5) (Murakami et al., 2015) using Amicon Ultra 15 centrifuge filters (Millipore). Purified protein was quantified using Bio-Rad protein assay reagent and diluted to 5 μg/μl in Droplet Buffer. Purified proteins were diluted (10% polyethylene glycol, 25 mM Tris, 75 mM NaCl pH 7.5) and visualized using a Zeiss LSM 710 confocal microscope. Images were acquired every 2 s for a total of 400 s.

Fluorescence recovery after photobleaching was performed on a LSM710 with a 63x objective lens. Photobleaching was attained with 50 scans of a 1 μm^2 region of interest of a droplet *in vitro*. Single plane images were collected at 1 s intervals. Recovery after photobleaching was calculated using ZEN software (Zeiss) after background subtraction, correction for fluorescence loss during image acquisition and normalization as described in (Boeynaems et al., 2017b).

Ex vivo GFP-TIAR-2 granules were visualized following dissociation of single cells from *juIs542* (*P_{mec-4}-GFP-TIAR-2)* expressing animals, as described in (Kaletsky et al., 2016). 50 μl of packed *juIs542* worms were permeabilized with lysis buffer (200 mM DTT, 0.25% SDS, 20 mM HEPES pH 8.0, 3% sucrose) and then dissociated with 20 mg/ml Pronase. Dissociated cells were resuspended in ~20 μl of M9, and 2 μl of the cell suspension was immediately imaged. Granules were visualized on a LSM710 with a 63X objective lens. Liquid-like granules were isolated on multiple occasions following single cell dissociation.

GFP Immunoprecipitation—500 μl of mixed stage worms expressing GFP fusion proteins in mechanosensory neurons were harvested and lysed in buffer (50 mM Tris pH 7.4, 100 mM NaCl, 1% NP-40, 0.1% SDS, 0.5% sodium deoxycholate) supplemented with protease inhibitors (Complete Ultra Tablets, Roche) and phosphatase inhibitors (PhosSTOP, Roche). GFP fusion proteins were immunoprecipitated using a μMACS GFP isolation kit (Miltenyi). Protein samples were run on SDS-PAGE for western blot analysis and probed with anti-phosphorylated serine (16B4, sc-81515, Santa Cruz Biotechnology) or

phosphorylated tyrosine (PY99, sc-7020, Santa Cruz Biotechnology) antibodies. Samples were probed with anti-GFP (ab290, Abcam) to determine the total amount of GFP protein immunoprecipitated.

Graphs and Statistical Analysis—All data are graphed using Prism v5.01 software (GraphPad, La Jolla, CA). Box and whisker plots show quartiles (box), median (line within box) and range (whiskers). Dot plots show individual data points (dots) and mean (horizontal line). Statistical significance was tested using Fisher's exact test, Students t-test, Mann-Whitney U Test or ANOVA with Tukey's post-test as appropriate. $P \geq 0.05$ was considered not significant (ns). $P \leq 0.05$ (*), $P \leq 0.01$ (**) and $P \leq 0.001$ (***) were considered significant differences. N values are indicated in the figures and figure legends.

Data and Code Availability

This study did not generate/analyze datasets or code.

Supplementary Material

Refer to Web version on PubMed Central for supplementary material.

Acknowledgements

We thank L. Toy, and F. Song, for strain construction, S. Koehler and A. Dernburg for protocols and technical advice on CRISPR/Cas9 mediated editing, K. McCulloch for advice on worm dissociation for single cell analysis, and M. Nonet for providing strains. We thank members of the Jin and Chisholm laboratories for valuable discussions and critical comments on the manuscript. Some strains were provided by the CGC, which is funded by NIH Office of Research Infrastructure Programs (P40 OD010440), and by the National Bioresource Project of Japan (S. Mitani). MGA was a Canadian Institutes of Health Research postdoctoral fellow (MFE-146808). MGA and YJ were partly supported by the Howard Hughes Medical Institute. This work was supported by an NIH grant R01 NS093588 (to YJ and ADC).

References

Alberti S, Gladfelter A, and Mittag T (2019). Considerations and Challenges in Studying Liquid-Liquid Phase Separation and Biomolecular Condensates. Cell 176, 419–434 [PubMed: 30682370]

Alberti S, Saha S, Woodruff JB, Franzmann TM, Wang J, and Hyman AA (2018). A User's Guide for Phase Separation Assays with Purified Proteins. J Mol Biol 430, 4806–4820 [PubMed: 29944854]

Anderson EN, Gochenaur L, Singh A, Grant R, Patel K, Watkins S, Wu JY, and Pandey UB (2018). Traumatic injury induces Stress Granule Formation and enhances Motor Dysfunctions in ALS/FTD Models. Hum Mol Genet 27, 1366–1381 [PubMed: 29432563]

Boeynaems S, Alberti S, Fawzi NL, Mittag T, Polymenidou M, Rousseau F, Schymkowitz J, Shorter J, Wolozin B, Van Den Bosch L, et al. (2018). Protein Phase Separation: A New Phase in Cell Biology. Trends Cell Biol 28, 420–435 [PubMed: 29602697]

Boeynaems S, Bogaert E, Kovacs D, Konijnenberg A, Timmerman E, Volkov A, Guharoy M, De Decker M, Jaspers T, Ryan VH, et al. (2017a). Phase Separation of C9orf72 Dipeptide Repeats Perturbs Stress Granule Dynamics. Mol Cell 65, 1044–1055 e1045 [PubMed: 28306503]

Boeynaems S, De Decker M, Tompa P, and Van Den Bosch L (2017b). Arginine-rich Peptides Can Actively Mediate Liquid-liquid Phase Separation. Bio-Protocol 7

Bracha D, Walls MT, Wei MT, Zhu L, Kurian M, Avalos JL, Toettcher JE, and Brangwynne CP (2018). Mapping Local and Global Liquid Phase Behavior in Living Cells Using Photo-Oligomerizable Seeds. Cell 175, 1467–1480 e1413 [PubMed: 30500534]

Bradke F, Fawcett JW, and Spira ME (2012). Assembly of a new growth cone after axotomy: the precursor to axon regeneration. Nat Rev Neurosci 13, 183–193 [PubMed: 22334213]

Brenner S (1974). The genetics of Caenorhabditis elegans. Genetics 77, 71–94 [PubMed: 4366476]

Buchan JR (2014). mRNP granules. Assembly, function, and connections with disease. RNA Biol 11, 1019–1030 [PubMed: 25531407]

Buchan JR, and Parker R (2009). Eukaryotic stress granules: the ins and outs of translation. Mol Cell 36, 932–941 [PubMed: 20064460]

Cartoni R, Norsworthy MW, Bei F, Wang C, Li S, Zhang Y, Gabel CV, Schwarz TL, and He Z (2016). The Mammalian-Specific Protein Armcx1 Regulates Mitochondrial Transport during Axon Regeneration. Neuron 92, 1294–1307 [PubMed: 28009275]

Cartoni R, Pekkurnaz G, Wang C, Schwarz TL, and He Z (2017). A high mitochondrial transport rate characterizes CNS neurons with high axonal regeneration capacity. PLoS One 12, e0184672 [PubMed: 28926622]

Chen L, Wang Z, Ghosh-Roy A, Hubert T, Yan D, O'Rourke S, Bowerman B, Wu Z, Jin Y, and Chisholm AD (2011). Axon regeneration pathways identified by systematic genetic screening in C. elegans. Neuron 71, 1043–1057 [PubMed: 21943602]

Chuang E, Hori AM, Hesketh CD, and Shorter J (2018). Amyloid assembly and disassembly. J Cell Sci 131

Damgaard CK, and Lykke-Andersen J (2011). Translational coregulation of 5'TOP mRNAs by TIA-1 and TIAR. Genes Dev 25, 2057–2068 [PubMed: 21979918]

Del Gatto-Konczak F, Bourgeois CF, Le Guiner C, Kister L, Gesnel MC, Stevenin J, and Breathnach R (2000). The RNA-binding protein TIA-1 is a novel mammalian splicing regulator acting through intron sequences adjacent to a 5' splice site. Mol Cell Biol 20, 6287–6299 [PubMed: 10938105]

Ding L, Spencer A, Morita K, and Han M (2005). The developmental timing regulator AIN-1 interacts with miRISCs and may target the argonaute protein ALG-1 to cytoplasmic P bodies in C. elegans. Mol Cell 19, 437–447 [PubMed: 16109369]

Eystathioy T, Jakymiw A, Chan EK, Seraphin B, Cougot N, and Fritzler MJ (2003). The GW182 protein colocalizes with mRNA degradation associated proteins hDcp1 and hLSm4 in cytoplasmic GW bodies. RNA 9, 1171–1173 [PubMed: 13130130]

Fay MM, Anderson PJ, and Ivanov P (2017). ALS/FTD-Associated C9ORF72 Repeat RNA Promotes Phase Transitions In Vitro and in Cells. Cell Rep 21, 3573–3584 [PubMed: 29262335]

Franks TM, and Lykke-Andersen J (2008). The control of mRNA decapping and P-body formation. Mol Cell 32, 605–615 [PubMed: 19061636]

Frokjaer-Jensen C, Davis MW, Hopkins CE, Newman BJ, Thummel JM, Olesen SP, Grunnet M, and Jorgensen EM (2008). Single-copy insertion of transgenes in Caenorhabditis elegans. Nat Genet 40, 1375–1383 [PubMed: 18953339]

Gasset-Rosa F, Lu S, Yu H, Chen C, Melamed Z, Guo L, Shorter J, Da Cruz S, and Cleveland DW (2019). Cytoplasmic TDP-43 De-mixing Independent of Stress Granules Drives Inhibition of Nuclear Import, Loss of Nuclear TDP-43, and Cell Death. Neuron 102, 339–357 e337 [PubMed: 30853299]

George SE, Simokat K, Hardin J, and Chisholm AD (1998). The VAB-1 Eph receptor tyrosine kinase functions in neural and epithelial morphogenesis in C. elegans. Cell 92, 633–643 [PubMed: 9506518]

Ghosh-Roy A, Goncharov A, Jin Y, and Chisholm AD (2012). Kinesin-13 and tubulin posttranslational modifications regulate microtubule growth in axon regeneration. Dev Cell 23, 716–728 [PubMed: 23000142]

Glebov OO, Cox S, Humphreys L, and Burrone J (2016). Neuronal activity controls transsynaptic geometry. Sci Rep 6, 22703 [PubMed: 26951792]

Gopal PP, Nirschl JJ, Klinman E, and Holzbaur EL (2017). Amyotrophic lateral sclerosis-linked mutations increase the viscosity of liquid-like TDP-43 RNP granules in neurons. Proc Natl Acad Sci U S A 114, E2466–E2475 [PubMed: 28265061]

Guzikowski AR, Chen YS, and Zid BM (2019). Stress-induced mRNP granules: Form and function of processing bodies and stress granules. Wiley Interdiscip Rev RNA 10, e1524 [PubMed: 30793528]

Hackman P, Sarparanta J, Lehtinen S, Vihola A, Evila A, Jonson PH, Luque H, Kere J, Screen M, Chinnery PF, et al. (2013). Welander distal myopathy is caused by a mutation in the RNA-binding protein TIA1. Ann Neurol 73, 500–509 [PubMed: 23401021]

Hammarlund M, and Jin Y (2014). Axon regeneration in C. elegans. Curr Opin Neurobiol 27, 199–207 [PubMed: 24794753]

Hammarlund M, Nix P, Hauth L, Jorgensen EM, and Bastiani M (2009). Axon regeneration requires a conserved MAP kinase pathway. Science 323, 802–806 [PubMed: 19164707]

Han SM, Baig HS, and Hammarlund M (2016). Mitochondria Localize to Injured Axons to Support Regeneration. Neuron 92, 1308–1323 [PubMed: 28009276]

Harrison AF, and Shorter J (2017). RNA-binding proteins with prion-like domains in health and disease. Biochem J 474, 1417–1438 [PubMed: 28389532]

He Z, and Jin Y (2016). Intrinsic Control of Axon Regeneration. Neuron 90, 437–451 [PubMed: 27151637]

Hofweber M, and Dormann D (2018). Friend or foe - post-translational modifications as regulators of phase separation and RNP granule dynamics. J Biol Chem

Hu BR, Martone ME, Jones YZ, and Liu CL (2000). Protein aggregation after transient cerebral ischemia. J Neurosci 20, 3191–3199 [PubMed: 10777783]

Huang S, Liu N, Li H, Zhao J, Su L, Zhang Y, Zhang S, Zhao B, and Miao J (2014). TIA1 interacts with annexin A7 in regulating vascular endothelial cell autophagy. Int J Biochem Cell Biol 57, 115–122 [PubMed: 25461769]

Hubert T, Wu Z, Chisholm AD, and Jin Y (2014). S6 kinase inhibits intrinsic axon regeneration capacity via AMP kinase in Caenorhabditis elegans. J Neurosci 34, 758–763 [PubMed: 24431434]

Huelgas-Morales G, Silva-Garcia CG, Salinas LS, Greenstein D, and Navarro RE (2016). The Stress Granule RNA-Binding Protein TIAR-1 Protects Female Germ Cells from Heat Shock in Caenorhabditis elegans. G3 (Bethesda) 6, 1031–1047 [PubMed: 26865701]

Jud MC, Czerwinski MJ, Wood MP, Young RA, Gallo CM, Bickel JS, Petty EL, Mason JM, Little BA, Padilla PA, et al. (2008). Large P body-like RNPs form in C. elegans oocytes in response to arrested ovulation, heat shock, osmotic stress, and anoxia and are regulated by the major sperm protein pathway. Dev Biol 318, 38–51 [PubMed: 18439994]

Kahl A, Blanco I, Jackman K, Baskar J, Milaganur Mohan H, Rodney-Sandy R, Zhang S, Iadecola C, and Hochrainer K (2018). Cerebral ischemia induces the aggregation of proteins linked to neurodegenerative diseases. Sci Rep 8, 2701 [PubMed: 29426953]

Kaletsky R, Lakhina V, Arey R, Williams A, Landis J, Ashraf J, and Murphy CT (2016). The C. elegans adult neuronal IIS/FOXO transcriptome reveals adult phenotype regulators. Nature 529, 92–96 [PubMed: 26675724]

Kato M, Han TW, Xie S, Shi K, Du X, Wu LC, Mirzaei H, Goldsmith EJ, Longgood J, Pei J, et al. (2012). Cell-free formation of RNA granules: low complexity sequence domains form dynamic fibers within hydrogels. Cell 149, 753–767 [PubMed: 22579281]

Kedersha NL, Gupta M, Li W, Miller I, and Anderson P (1999). RNA-binding proteins TIA-1 and TIAR link the phosphorylation of eIF-2 alpha to the assembly of mammalian stress granules. J Cell Biol 147, 1431–1442 [PubMed: 10613902]

Kim KW, Tang NH, Piggott CA, Andrusiak MG, Park S, Zhu M, Kurup N, Cherra SJ 3rd, Wu Z, Chisholm AD, et al. (2018). Expanded genetic screening in Caenorhabditis elegans identifies new regulators and an inhibitory role for NAD(+) in axon regeneration. Elife 7

Klar J, Sobol M, Melberg A, Mabert K, Ameur A, Johansson AC, Feuk L, Entesarian M, Orlen H, Casar-Borota O, et al. (2013). Welander distal myopathy caused by an ancient founder mutation in TIA1 associated with perturbed splicing. Hum Mutat 34, 572–577 [PubMed: 23348830]

Knowlton WM, Hubert T, Wu Z, Chisholm AD, and Jin Y (2017). A Select Subset of Electron Transport Chain Genes Associated with Optic Atrophy Link Mitochondria to Axon Regeneration in Caenorhabditis elegans. Front Neurosci 11, 263 [PubMed: 28539870]

Lancaster AK, Nutter-Upham A, Lindquist S, and King OD (2014). PLAAC: a web and command-line application to identify proteins with prion-like amino acid composition. Bioinformatics 30, 2501–2502 [PubMed: 24825614]

Larson AG, Elnatan D, Keenen MM, Trnka MJ, Johnston JB, Burlingame AL, Agard DA, Redding S, and Narlikar GJ (2017). Liquid droplet formation by HP1alpha suggests a role for phase separation in heterochromatin. Nature 547, 236–240 [PubMed: 28636604]

Lechler MC, Crawford ED, Groh N, Widmaier K, Jung R, Kirstein J, Trinidad JC, Burlingame AL, and David DC (2017). Reduced Insulin/IGF-1 Signaling Restores the Dynamic Properties of Key Stress Granule Proteins during Aging. Cell Rep 18, 454–467 [PubMed: 28076789]

Li Y, Andereggen L, Yuki K, Omura K, Yin Y, Gilbert HY, Erdogan B, Asdourian MS, Shrock C, de Lima S, et al. (2017). Mobile zinc increases rapidly in the retina after optic nerve injury and regulates ganglion cell survival and optic nerve regeneration. Proc Natl Acad Sci U S A 114, E209–E218 [PubMed: 28049831]

Lin Y, Currie SL, and Rosen MK (2017). Intrinsically disordered sequences enable modulation of protein phase separation through distributed tyrosine motifs. J Biol Chem 292, 19110–19120 [PubMed: 28924037]

Lin Y, Protter DS, Rosen MK, and Parker R (2015). Formation and Maturation of Phase-Separated Liquid Droplets by RNA-Binding Proteins. Mol Cell 60, 208–219 [PubMed: 26412307]

Mackenzie IR, Nicholson AM, Sarkar M, Messing J, Purice MD, Pottier C, Annu K, Baker M, Perkerson RB, Kurti A, et al. (2017). TIA1 Mutations in Amyotrophic Lateral Sclerosis and Frontotemporal Dementia Promote Phase Separation and Alter Stress Granule Dynamics. Neuron 95, 808–816 e809 [PubMed: 28817800]

Mello CC, Kramer JM, Stinchcomb D, and Ambros V (1991). Efficient gene transfer in C.elegans: extrachromosomal maintenance and integration of transforming sequences. EMBO J 10, 3959–3970 [PubMed: 1935914]

Milovanovic D, Wu Y, Bian X, and De Camilli P (2018). A liquid phase of synapsin and lipid vesicles. Science 361, 604–607 [PubMed: 29976799]

Monahan Z, Ryan VH, Janke AM, Burke KA, Rhoads SN, Zerze GH, O'Meally R, Dignon GL, Conicella AE, Zheng W, et al. (2017). Phosphorylation of the FUS low-complexity domain disrupts phase separation, aggregation, and toxicity. EMBO J 36, 2951–2967 [PubMed: 28790177]

Murakami T, Qamar S, Lin JQ, Schierle GS, Rees E, Miyashita A, Costa AR, Dodd RB, Chan FT, Michel CH, et al. (2015). ALS/FTD Mutation-Induced Phase Transition of FUS Liquid Droplets and Reversible Hydrogels into Irreversible Hydrogels Impairs RNP Granule Function. Neuron 88, 678–690 [PubMed: 26526393]

Nix P, Hammarlund M, Hauth L, Lachnit M, Jorgensen EM, and Bastiani M (2014). Axon regeneration genes identified by RNAi screening in C. elegans. J Neurosci 34, 629–645 [PubMed: 24403161]

Paix A, Folkmann A, Rasoloson D, and Seydoux G (2015). High Efficiency, Homology-Directed Genome Editing in Caenorhabditis elegans Using CRISPR-Cas9 Ribonucleoprotein Complexes. Genetics 201, 47–54 [PubMed: 26187122]

Paix A, Wang Y, Smith HE, Lee CY, Calidas D, Lu T, Smith J, Schmidt H, Krause MW, and Seydoux G (2014). Scalable and versatile genome editing using linear DNAs with microhomology to Cas9 Sites in Caenorhabditis elegans. Genetics 198, 1347–1356 [PubMed: 25249454]

Patel A, Malinovska L, Saha S, Wang J, Alberti S, Krishnan Y, and Hyman AA (2017). ATP as a biological hydrotrope. Science 356, 753–756 [PubMed: 28522535]

Qamar S, Wang G, Randle SJ, Ruggeri FS, Varela JA, Lin JQ, Phillips EC, Miyashita A, Williams D, Strohl F, et al. (2018). FUS Phase Separation Is Modulated by a Molecular Chaperone and Methylation of Arginine Cation-pi Interactions. Cell 173, 720–734 e715 [PubMed: 29677515]

Rayman JB, Karl KA, and Kandel ER (2018). TIA-1 Self-Multimerization, Phase Separation, and Recruitment into Stress Granules Are Dynamically Regulated by Zn(2). Cell Rep 22, 59–71 [PubMed: 29298433]

Rieckher M, Markaki M, Princz A, Schumacher B, and Tavernarakis N (2018). Maintenance of Proteostasis by P Body-Mediated Regulation of eIF4E Availability during Aging in Caenorhabditis elegans. Cell Rep 25, 199–211 e196 [PubMed: 30282029]

Rieckher M, and Tavernarakis N (2017). P-body and Stress Granule Quantification in Caenorhabditis elegans. Bio Protoc 7

Sahoo PK, Lee SJ, Jaiswal PB, Alber S, Kar AN, Miller-Randolph S, Taylor EE, Smith T, Singh B, Ho TS, et al. (2018). Axonal G3BP1 stress granule protein limits axonal mRNA translation and nerve regeneration. Nat Commun 9, 3358 [PubMed: 30135423]

Sanchez-Jimenez C, and Izquierdo JM (2015). T-cell intracellular antigens in health and disease. Cell Cycle 14, 2033–2043 [PubMed: 26036275]

Schindelin J, Arganda-Carreras I, Frise E, Kaynig V, Longair M, Pietzsch T, Preibisch S, Rueden C, Saalfeld S, Schmid B, et al. (2012). Fiji: an open-source platform for biological-image analysis. Nat Methods 9, 676–682 [PubMed: 22743772]

Shin Y, and Brangwynne CP (2017). Liquid phase condensation in cell physiology and disease. Science 357

Silva-Garcia CG, and Estela Navarro R (2013). The C. elegans TIA-1/TIAR homolog TIAR-1 is required to induce germ cell apoptosis. Genesis 51, 690–707 [PubMed: 23913578]

Sun Y, Yang P, Zhang Y, Bao X, Li J, Hou W, Yao X, Han J, and Zhang H (2011). A genome-wide RNAi screen identifies genes regulating the formation of P bodies in C. elegans and their functions in NMD and RNAi. Protein Cell 2, 918–939 [PubMed: 22180091]

Thomas MG, Martinez Tosar LJ, Desbats MA, Leishman CC, and Boccaccio GL (2009). Mammalian Staufen 1 is recruited to stress granules and impairs their assembly. J Cell Sci 122, 563–573 [PubMed: 19193871]

Tinevez JY, Perry N, Schindelin J, Hoopes GM, Reynolds GD, Laplantine E, Bednarek SY, Shorte SL, and Eliceiri KW (2017). TrackMate: An open and extensible platform for single-particle tracking. Methods 115, 80–90 [PubMed: 27713081]

Tourriere H, Chebli K, Zekri L, Courselaud B, Blanchard JM, Bertrand E, and Tazi J (2003). The RasGAP-associated endoribonuclease G3BP assembles stress granules. J Cell Biol 160, 823–831 [PubMed: 12642610]

Trakhtenberg EF, Li Y, Feng Q, Tso J, Rosenberg PA, Goldberg JL, and Benowitz LI (2018). Zinc chelation and Klf9 knockdown cooperatively promote axon regeneration after optic nerve injury. Exp Neurol 300, 22–29 [PubMed: 29106981]

Uryu K, Chen XH, Martinez D, Browne KD, Johnson VE, Graham DI, Lee VM, Trojanowski JQ, and Smith DH (2007). Multiple proteins implicated in neurodegenerative diseases accumulate in axons after brain trauma in humans. Exp Neurol 208, 185–192 [PubMed: 17826768]

Van Treeck B, and Parker R (2019). Principles of Stress Granules Revealed by Imaging Approaches. Cold Spring Harb Perspect Biol 11

Vernon RM, Chong PA, Tsang B, Kim TH, Bah A, Farber P, Lin H, and Forman-Kay JD (2018). Pi-Pi contacts are an overlooked protein feature relevant to phase separation. Elife 7

Wang A, Conicella AE, Schmidt HB, Martin EW, Rhoads SN, Reeb AN, Nourse A, Ramirez Montero D, Ryan VH, Rohatgi R, et al. (2018a). A single N-terminal phosphomimic disrupts TDP-43 polymerization, phase separation, and RNA splicing. EMBO J 37

Wang J, Choi JM, Holehouse AS, Lee HO, Zhang X, Jahnel M, Maharana S, Lemaitre R, Pozniakovsky A, Drechsel D, et al. (2018b). A Molecular Grammar Governing the Driving Forces for Phase Separation of Prion-like RNA Binding Proteins. Cell 174, 688–699 e616 [PubMed: 29961577]

Wang X, Roy PJ, Holland SJ, Zhang LW, Culotti JG, and Pawson T (1999). Multiple ephrins control cell organization in C. elegans using kinase-dependent and -independent functions of the VAB-1 Eph receptor. Mol Cell 4, 903–913 [PubMed: 10635316]

Wu D, Lee S, Luo J, Xia H, Gushchina S, Richardson PM, Yeh J, Krugel U, Franke H, Zhang Y, et al. (2018). Intraneural Injection of ATP Stimulates Regeneration of Primary Sensory Axons in the Spinal Cord. J Neurosci 38, 1351–1365 [PubMed: 29279307]

Wu Z, Ghosh-Roy A, Yanik MF, Zhang JZ, Jin Y, and Chisholm AD (2007). Caenorhabditis elegans neuronal regeneration is influenced by life stage, ephrin signaling, and synaptic branching. Proc Natl Acad Sci U S A 104, 15132–15137 [PubMed: 17848506]

Yan D, Wu Z, Chisholm AD, and Jin Y (2009). The DLK-1 kinase promotes mRNA stability and local translation in C. elegans synapses and axon regeneration. Cell 138, 1005–1018 [PubMed: 19737525]

Yanik MF, Cinar H, Cinar HN, Chisholm AD, Jin Y, and Ben-Yakar A (2004). Neurosurgery: functional regeneration after laser axotomy. Nature 432, 822 [PubMed: 15602545]

Zhang P, Fan B, Yang P, Temirov J, Messing J, Kim HJ, and Taylor JP (2019). Chronic optogenetic induction of stress granules is cytotoxic and reveals the evolution of ALS-FTD pathology. Elife 8

Zhang T, Delestienne N, Huez G, Kruys V, and Gueydan C (2005). Identification of the sequence determinants mediating the nucleo-cytoplasmic shuttling of TIAR and TIA-1 RNA-binding proteins. J Cell Sci 118, 5453–5463 [PubMed: 16278295]

Zheng Q, Ahlawat S, Schaefer A, Mahoney T, Koushika SP, and Nonet ML (2014). The vesicle protein SAM-4 regulates the processivity of synaptic vesicle transport. PLoS Genet 10, e1004644 [PubMed: 25329901]

Zhou B, Yu P, Lin MY, Sun T, Chen Y, and Sheng ZH (2016). Facilitation of axon regeneration by enhancing mitochondrial transport and rescuing energy deficits. J Cell Biol 214, 103–119 [PubMed: 27268498]

Zhou K, Cherra SJ 3rd, Goncharov A, and Jin Y (2017). Asynchronous Cholinergic Drive Correlates with Excitation-Inhibition Imbalance via a Neuronal Ca(2+) Sensor Protein. Cell Rep 19, 1117–1129 [PubMed: 28494862]

Highlights

- The *C. elegans* TIA family protein TIAR-2 is an intrinsic inhibitor of axon regeneration
- TIAR-2 undergoes liquid-liquid phase separation *in vitro,* and axonal TIAR-2 granules display liquid-like properties *in vivo.*
- The prion-like domain of TIAR-2 is necessary and sufficient for granule formation and its function in axon regeneration
- Tyrosine and serine residues within the PrLD are critical for granule formation and the function of TIAR-2 in axon injury

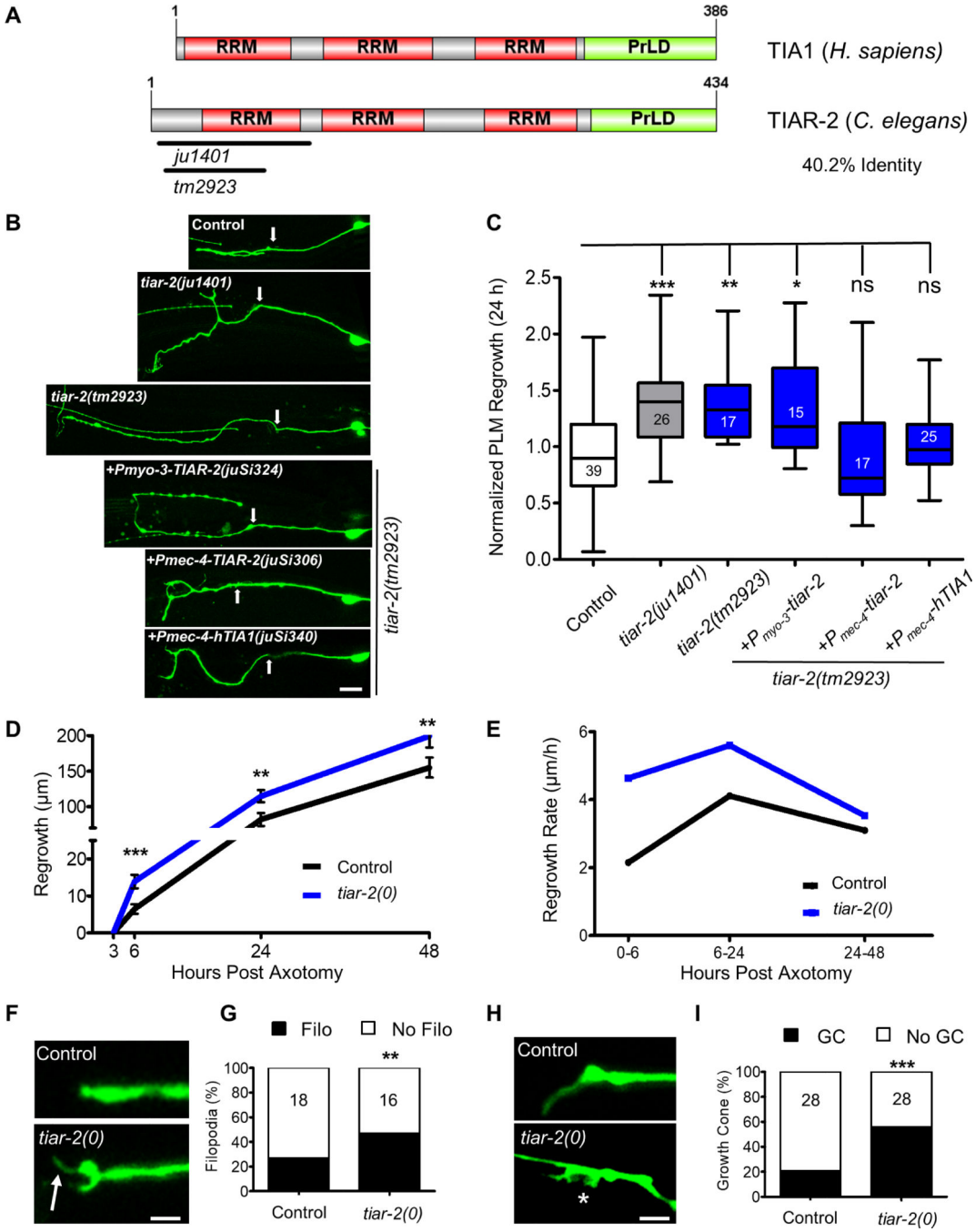

Figure 1: *tiar-2* is an intrinsic inhibitor of axon regeneration

A) *C. elegans* TIAR-2(Q9U2F5) has high sequence identity with human TIA1(P31483). TIA proteins consist of three RNA-recognition motifs (RRM) and a C-terminal prion-like domain (PrLD). The PrLD was determined using the Prion-Like Amino Acid Composition (PLAAC) algorithm (Lancaster et al., 2014). Percent identity was calculated for full-length proteins using Clustal Omega (http://www.ebi.ac.uk/Tools/msa/clustalo/). *tiar-2* deletion alleles (*ju1401* and *tm2923)* are indicated below TIAR-2.

B) Representative confocal images of PLM axon regrowth 24 h post-axotomy in animals expressing *zdIs5* [$P_{mec\text{-}4}$-*GFP*]. Genotypes in the top three images are as indicated, and those in the bottom three are in a *tiar-2(tm2923)* background with the transgenes indicated. Arrows indicate the site of axon injury. Scale bar, 10 μm.

C) Quantification of PLM axon regrowth 24 h post-axotomy, normalized to same-day controls, is shown as a box and whisker plot. Number indicates animals analyzed. One-way ANOVA with Tukey's post-hoc test; *$P < 0.05$; **$P < 0.01$; ***P<0.001; ns, not significant.

D) PLM regrowth length over 48 h post-axotomy. Data points show mean ± SEM. Number of animals analyzed for 3, 6, 24 and 48 h: control (16, 28, 18, 16) and *tiar-2(0)* (18, 28, 17, 17). One-way ANOVA with Tukey's post hoc test; **$P < 0.01$; ***$P < 0.001$

E) Axon regrowth rate of PLM neurons at the indicated intervals following axotomy.

F) Representative confocal images of PLM axons 3 h post-axotomy. Arrow marks filopodia in *tiar-2(0)*. Scale bar, 2 μm.

G) Quantification of axons with filopodia (Filo) as %, 3 h post-axotomy. Number indicates animals analyzed. Fisher's exact test; **$P < 0.01$.

H) Representative confocal images of PLM axons 6 h post-axotomy. Asterisks marks growth cone in *tiar-2(0)*. Scale bar, 2 μm.

I) Quantification of axons with growth cones (GC) as %, 6 h post-axotomy. Number indicates animals analyzed. Fisher's exact test; ***$P < 0.001$.

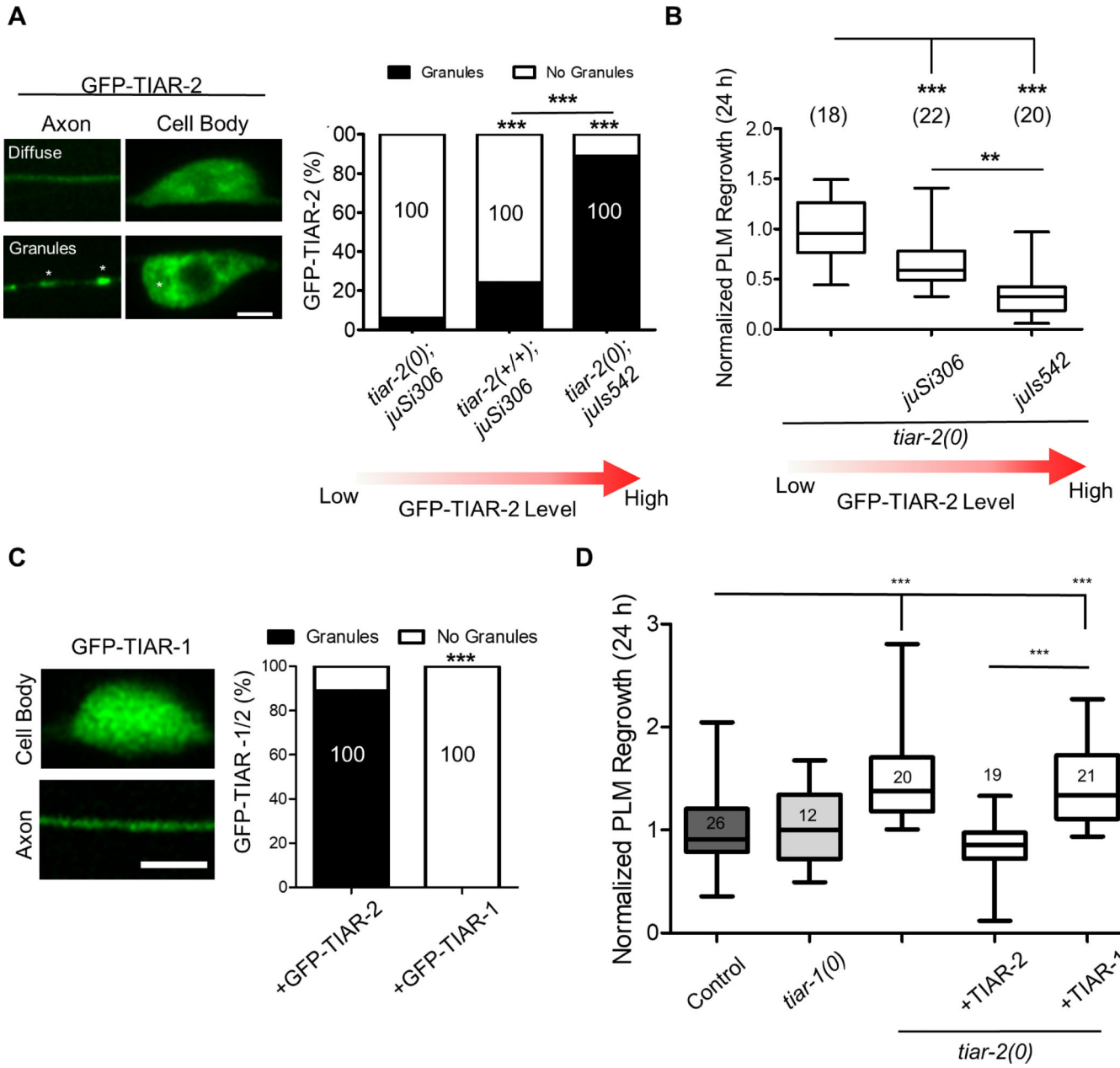

Figure 2. TIAR-2 forms granules *in vivo* and overexpression of TIAR-2 inhibits axon regeneration

A) Left: Representative confocal images of GFP-TIAR-2 expression from a single-copy insertion transgene [*juSi306*] in a PLM axon. Asterisks (*) denote granules; Scale bar, 3 μm. Right: Graph shows quantification of PLM axons containing granules as %, Number indicates neurons scored. Fisher's exact test; ***$P < 0.001$.

B) Axon regrowth of PLM neurons 24 h post-axotomy, normalized to same-day *tiar-2(0)* animals, shown as a box and whisker plot. Number indicates animals analyzed. One-way ANOVA with Tukey's post-hoc test; **$P < 0.01$; ***$P < 0.001$.

C) Left: Representative confocal images show that GFP-TIAR-1[*juEx7943*] in mechanosensory neurons does not form granules, when expressed at similar levels as GFP-

TIAR-2[*juIs542*]. Right: Graph shows quantification of PLM axons containing granules. Number indicates neurons scored. Fisher's exact test; ***$P < 0.001$.
D) Quantification of PLM axon regrowth 24 h post-axotomy, normalized to same-day controls, shown as a box and whisker plot. Number indicates animals analyzed. One-way ANOVA with Tukey's post-hoc test; ***P<0.001; ns, not significant.

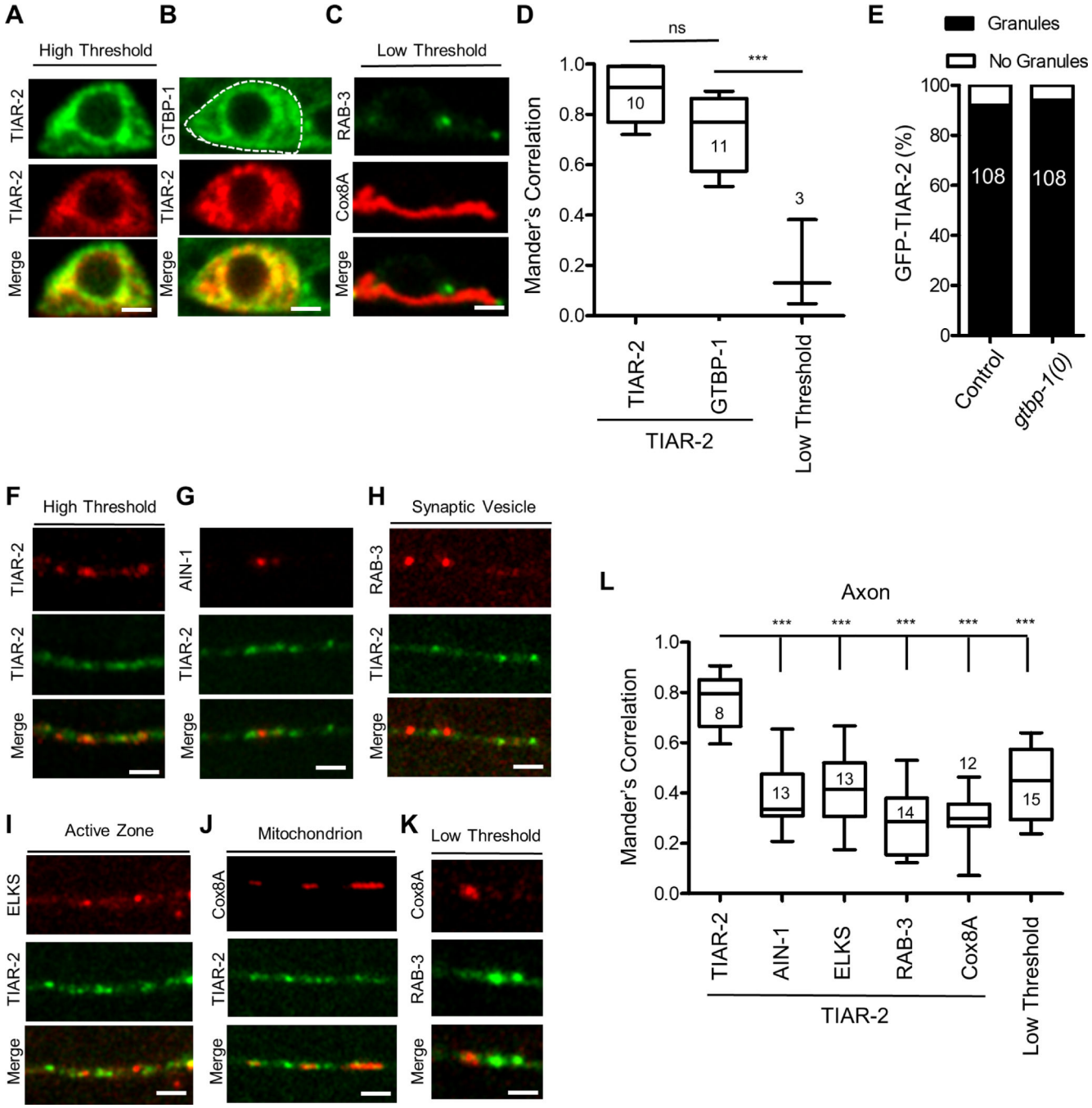

Figure 3. TIAR-2 granules in neurons are likely heterogenous

A) Representative confocal images showing mKate2-TIAR-2[*juEx8008*] granules colocalizes with GFP-TIAR-2[*juIs542*] granules in the PLM cell body. Scale 2 μm.

B) Representative confocal images showing mKate2-TIAR-2[*juEx8008*] granules partially colocalize with GTBP-1-GFP[*ax2053*] granules in the PLM cell body. Scale 2 μm.

C) Representative confocal images showing GFP-RAB-3[*jsIs821*] does not colocalize with tagRFP-Cox8A[*jsIs1073*] granules in the PLM cell body. Scale 2 μm.

D) Quantification of colocalization for mKate2-TIAR-2 and GTBP-1-GFP, shown as a box and whisker plot. One-way ANOVA with Tukey's post-hoc test; ***P<0.001; ns, not significant.

E) Graph shows quantification of PLM axons containing GFP-TIAR-2[*juIs542*] granules in control and *gtbp-1(0)* backgrounds. Number indicates neurons scored.

F) Representative confocal images showing GFP-TIAR-2[*juIs542*] granules colocalize with mKate2-TIAR-2[*juEx8008*]. Scale 2 μm.

G) Representative confocal images showing GFP-TIAR-2[*juIs542*] granules do not colocalize with granules of mKate2-AIN-1[*juEx7948*] in the PLM axon. Scale 2 μm.

H) Representative confocal images showing GFP-TIAR-2[*juIs542*] granules do not colocalize with the synaptic vesicle marker tagRFP-RAB-3[*jsIs1263*] in the PLM axon. Scale 2 μm.

I) Representative confocal images showing GFP-TIAR-2[*juIs542*] granules do not colocalize with the active zone marker tagRFP-ELKS[*jsIs1075*] in the PLM axon Scale 2 μm.

J) Representative confocal images showing GFP-TIAR-2[*juIs542*] granules do not colocalize with the mitochondrial marker tagRFP-Cox8A[*jsIs1073*] in the PLM axon. Scale 2 μm.

K) Representative confocal images showing GFP-RAB-3[*jsIs821*], a synaptic vesicle marker, displays minimal colocalization with tagRFP-Cox8A[*jsIs1073*], a mitochondrial marker, in the PLM cell body. Scale 2 μm.

L) Quantification of colocalization for the above red and green fluorescent tagged proteins, shown as a box and whisker plot. One-way ANOVA with Tukey's post-hoc test; ***P<0.001; ns, not significant.

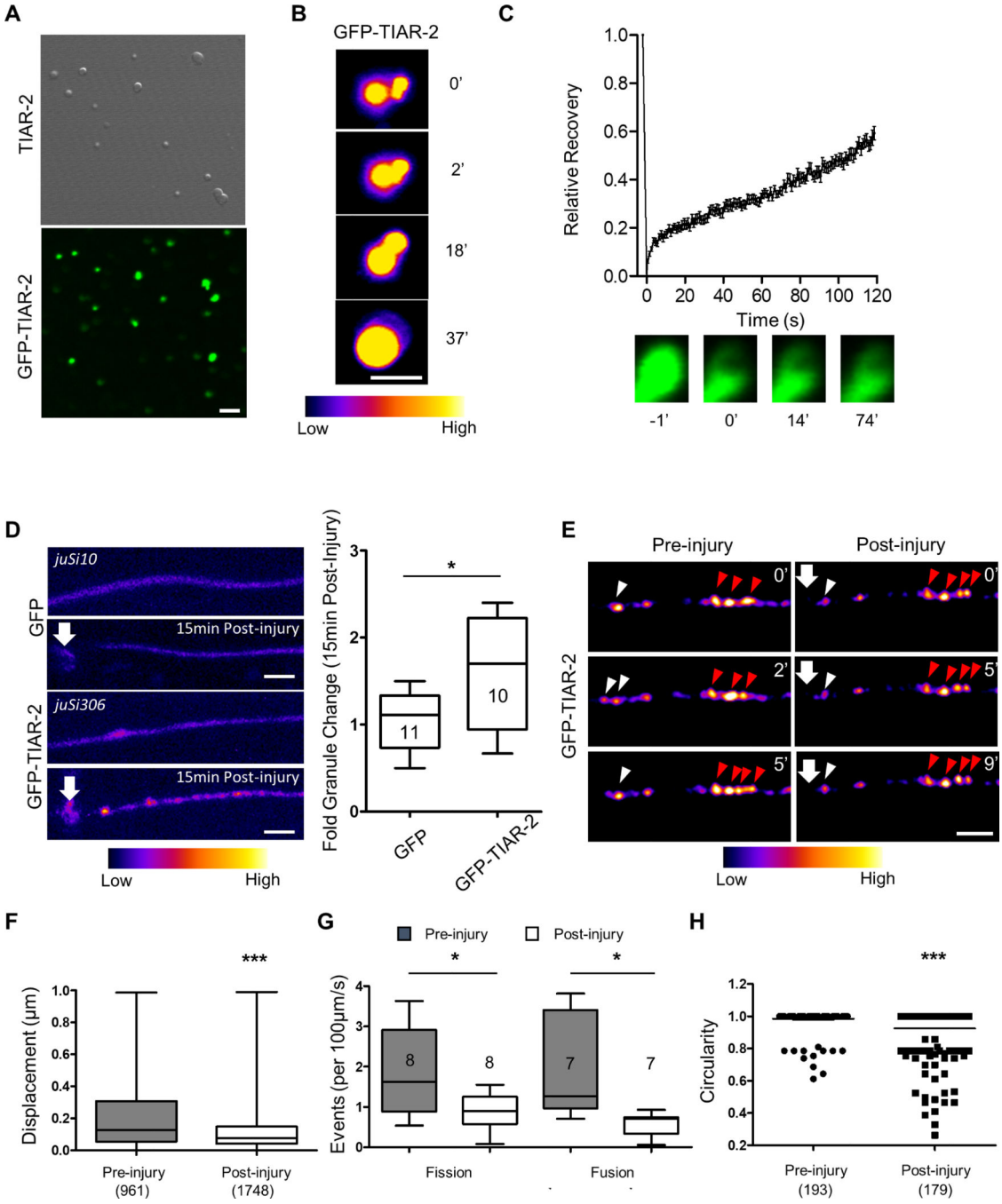

Figure 4. TIAR-2 undergoes liquid-liquid phase separation *in vitro* and forms granules with liquid-like features *in vivo* which change dynamics and increase in number following injury

A) Representative confocal images showing purified TIAR-2 and GFP-TIAR-2 liquid droplets, with 5 µg/µl purified protein supplemented with 10% PEG at room temperature. Scale bar, 2 µm.

B) Representative confocal images showing purified GFP-TIAR-2 liquid droplets fusing. Images were pseudo-colored using the 'Fire' lookup table in FIJI. Scale bar, 5 µm.

C) Relative fluorescence recovery (Y-axis) after photobleaching of purified GFP-TIAR-2 at the times indicated in the X-axis quantified using ZEN software and graphed with Prism

V5.01. Representative images of GFP-TIAR-2 before and after photobleaching are shown below.

D) Left: Representative confocal images show GFP[*juSi10*] and GFP-TIAR-2[*juSi306*] in PLM axons before and after axotomy. Images were pseudo-colored using the 'Fire' lookup table in FIJI. Arrow indicates the site of axon injury. Scale bar, 5 μm. Right: Quantification of GFP [*juSi10*] and GFP-TIAR-2[*juSi306*] granules 15min following axotomy, shown as a box and whisker plot. Number indicates animals analyzed. Student's t-test, $*P < 0.05$.

E) Representative spinning-disc confocal images of GFP-TIAR-2 [*juIs542*] in a PLM axon before and immediately after axotomy. Images were pseudo-colored using the 'Fire' lookup table in FIJI. White arrowhead marks granules undergoing a fusion event, whereas red arrowheads indicate granules undergoing fission, white arrows mark the site of axotomy. Scale bar, 2 μm.

F) Quantification of net displacement of GFP-TIAR-2[*juIs542*] granules before and after axotomy, shown as a box and whisker plot. Number is granules analyzed, from 5 animals. Mann-Whitney U-Test, ***P<0.001.

G) Quantification of GFP-TIAR-2[*juIs542*] granule fission and fusion events before and after axotomy, shown as box and whisker plot. Number indicates animals analyzed. Student's T-test, $*P < 0.05$.

H) Quantification of circularity of GFP-TIAR-2[*juIs542*] granules before and 15 min following axotomy, shown as a dot plot. Number is the number of granules analyzed, from 7 animals. Mann-Whitney U Test, $***P < 0.001$.

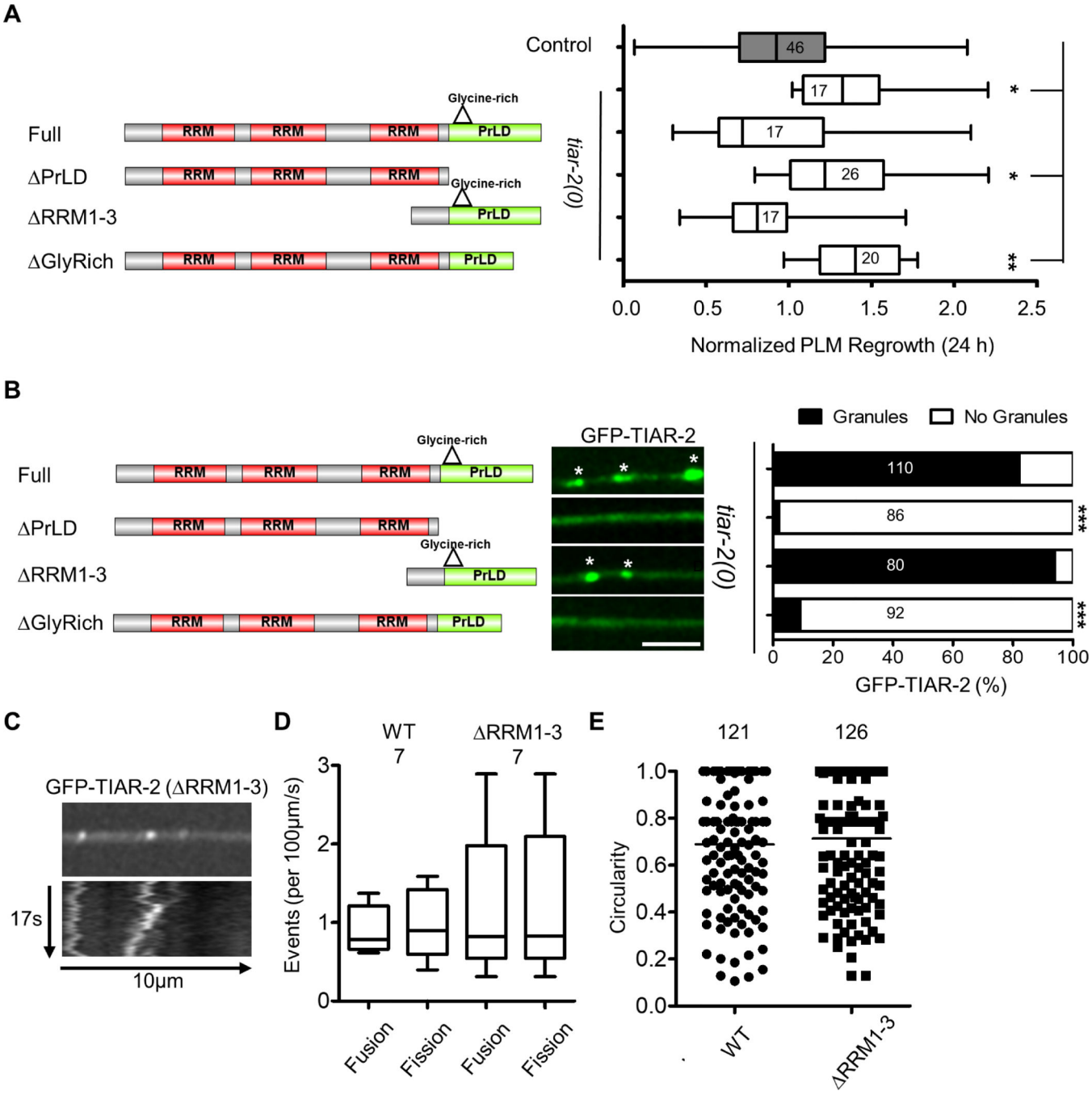

Figure 5: The PrLD of TIAR-2 is necessary and sufficient for function in axon regeneration and for granule formation

A) Left: Schematics show GFP-TIAR-2 truncation mutants. Right: Quantification of the effects of TIAR-2 variants on axon regrowth using single-copy expression transgenes in a *tiar-2(0)* background, shown as a box and whisker plot. Number indicates animals analyzed. One-way ANOVA with Tukey's post-hoc test; $*P < 0.05$; $**P < 0.01$.

B) Left: Schematics of GFP-TIAR-2 truncation mutants. Middle: Representative confocal images of corresponding GFP-TIAR-2 expressed from multi-copy transgenes in PLM axons. Asterisks (*) denotes granules, Scale bar, 5 μm. Right: Quantification of PLM axons

containing granules as %, Number indicates neurons scored. Fisher's exact test; ***$P <$ 0.001.

C) Representative spinning disc confocal image (top) and kymograph (bottom) of GFP-TIAR-2 (ΔRRM1–3) in a PLM axon. Kymograph depicts 17 s of spinning disc imaging over 10 μm of axon.

D) Quantification of GFP-TIAR-2(ΔRRM1–3)[*juEx7864/7865*] granule fission and fusion events, shown as a box and whisker plot. Number indicates animals analyzed.

E) Quantification of circularity of GFP-TIAR-2(ΔRRM1–3)[*juEx7864/7865*] granules. Data shown as a dot plot. Number is granules analyzed, from 7 animals.

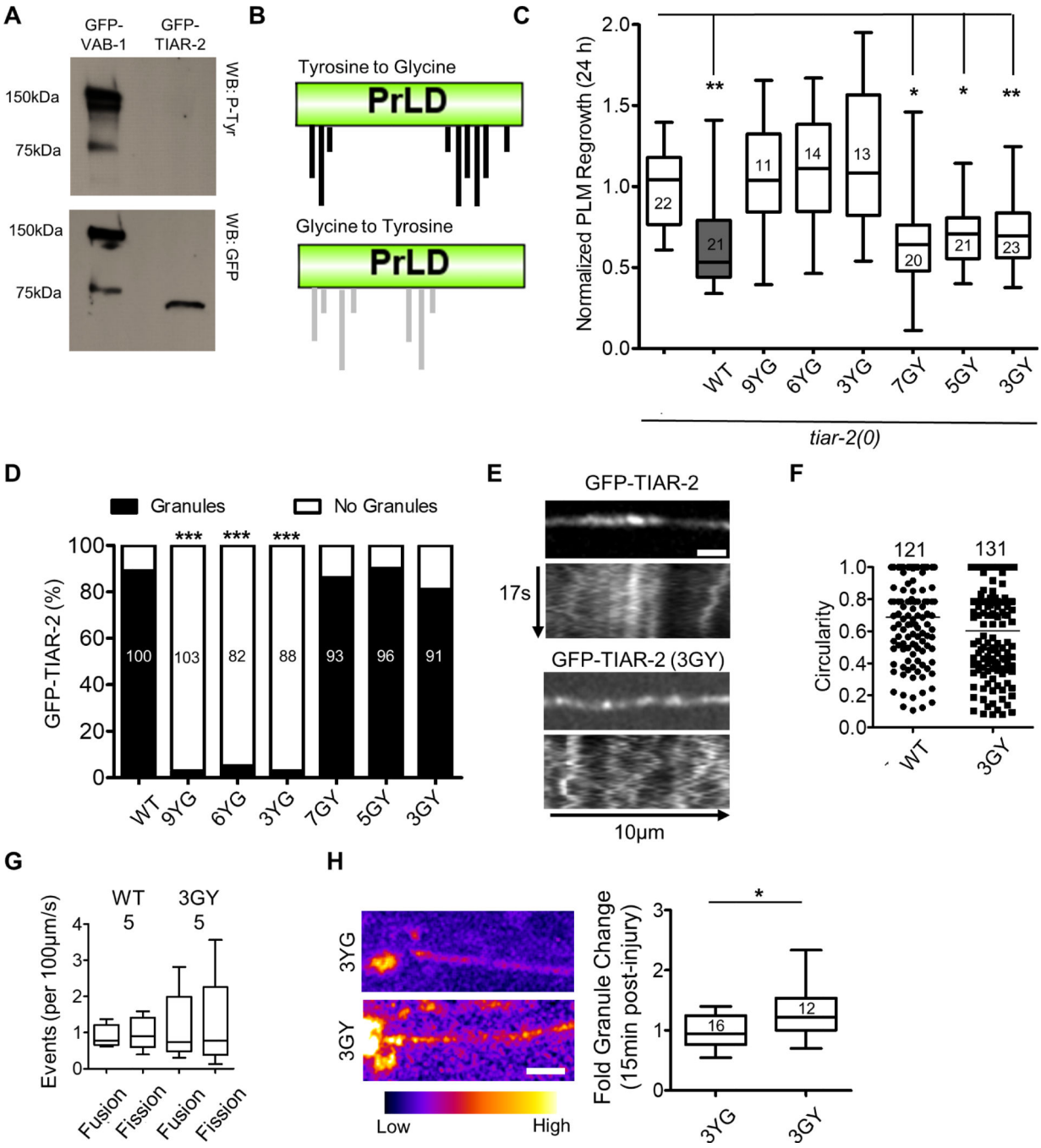

Figure 6. Tyrosine residues in the PrLD of TIAR-2 regulate granule formation and activity in regeneration

A) Tyrosine phosphorylation of GFP-TIAR-2 is undetectable in mechanosensory neurons. Protein extracts were isolated from *tiar-2(0); juSi306(P$_{mec-4}$-GFP-TIAR-2),* and *juIs24(VAB-1-GFP)* animals, immunoprecipitated with anti-GFP and analyzed by western blot with antibodies recognizing phosphorylated tyrosine (top) and GFP (bottom). Predicted molecular weight: ~74 kDa for GFP-TIAR-2 and ~150 kDa for VAB-1-GFP.

B) Schematics show the PrLD of TIAR-2 (Q9U2F5) with black lines (top) indicating Y>G mutations, and grey lines (bottom) for G>Y. Shortest lines represent the 3YG/3GY

mutations, medium 6YG/5GY, and the longest 9YG/7GY. Mutations in shorter constructs are contained in the larger variants.

C) Quantification of the effects of TIAR-2 tyrosine variants on axon regrowth using single-copy expression transgenes in a *tiar-2(0)* background, shown as a box and whisker plot. Number indicates animals analyzed. One-way ANOVA with Tukey's post-hoc test; $*P < 0.05$; $**P < 0.01$.

D) Graph shows quantification of PLM axons containing granules as %. Number indicates neurons scored. Fisher's exact test; $***P < 0.001$.

E) Representative spinning disc confocal image (top) and kymograph (bottom) of GFP-TIAR-2[*juSi542*] and GFP-TIAR-2(3GY)[*juEx7980*] in a PLM axon. Kymograph was created using 17 s of spinning disc imaging and 10 μm of axon.

F) Quantification of circularity of GFP-TIAR-2[*juSi542*] and GFP-TIAR-2(3GY)[*juEx7980/7981*]granules, shown as a dot plot. Number is granules analyzed, from 7 animals.

G) Quantification of fission and fusion events of GFP-TIAR-2[*juSi542*] and GFP-TIAR-2(3GY)[*juEx7980/7981*] granules, shown as a box and whisker plot. Number indicates animals analyzed.

H) Left: Representative confocal images of GFP-TIAR-2(3YG)[*juSi385*] and (3GY)[*juSi381*] 15 min post-axotomy. 'Fire' Lookup table used for visualization of intensity changes. Scale 2 μm. Arrow marks the site of axon injury. Right: Quantification of GFP-TIAR-2(3YG) and (3GY) granules 15min following axotomy, shown as a box and whisker plot. Number indicates animals analyzed. Unpaired Student's T-test; $*P < 0.05$.

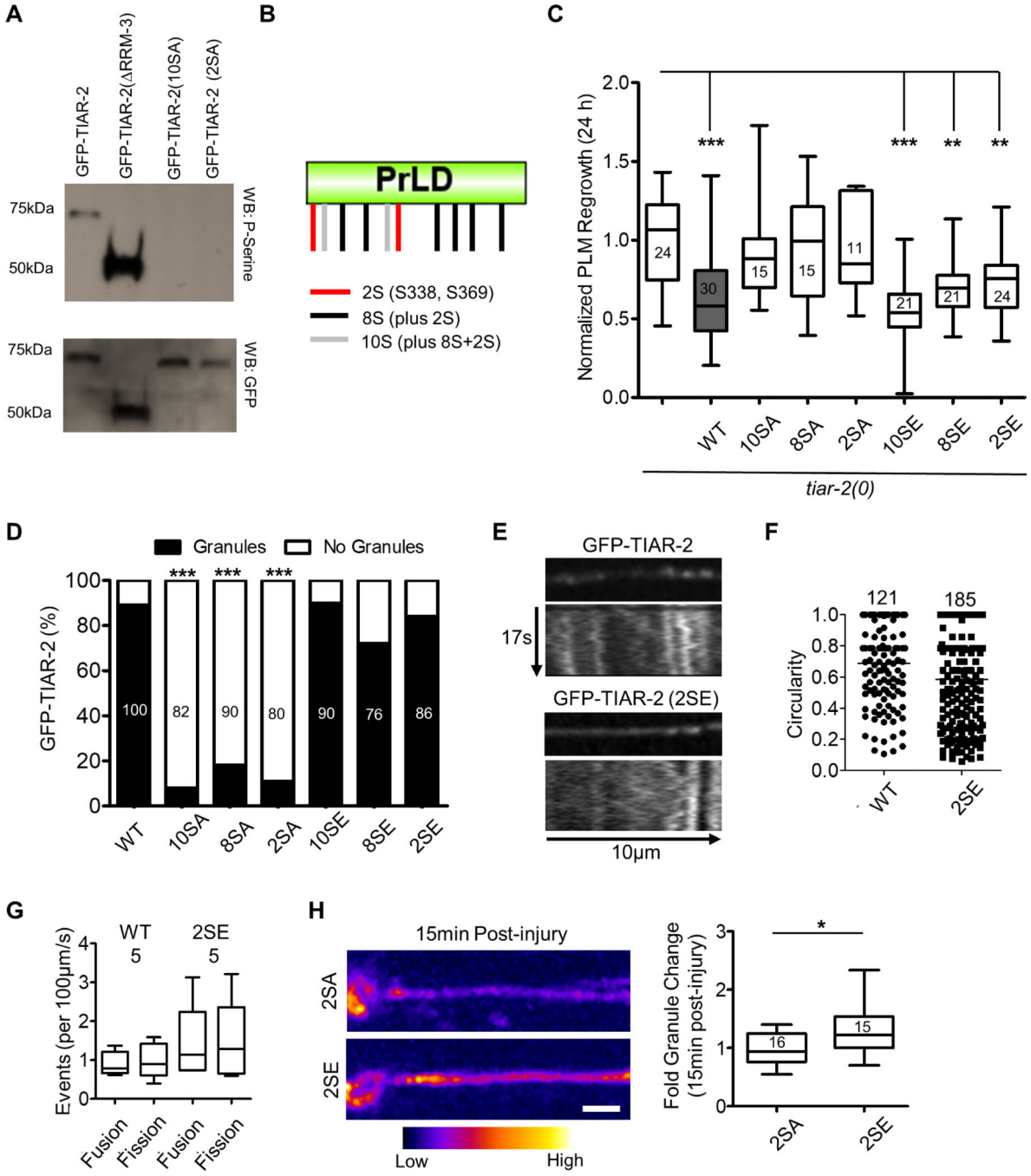

Figure 7. Serine residues in the PrLD of TIAR-2 regulate granule formation and activity in regeneration

A) GFP-TIAR-2 in mechanosensory neurons is phosphorylated. Protein extracts were isolated from *tiar-2(0); juSi306(*$P_{mec\text{-}4}$*-GFP-TIAR-2), tiar-2(0); juSi307(*$P_{mec\text{-}4}$*-GFP-TIAR-2 (ΔRRM1–3), tiar-2(0); juSi376(*$P_{mec\text{-}4}$*-GFP-TIAR-2(10SA)),* and *tiar-2(0); juSi374(*$P_{mec\text{-}4}$*-GFP-TIAR-2*(2SA)) animals, immunoprecipitated with anti-GFP and analyzed by western blot with antibodies recognizing phosphorylated serine (top) and GFP (bottom). GFP-TIAR-2 has a predicted molecular weight of ~74 kDa and GFP-TIAR-2(Δ*RRM1–3)* ~45 kDa.

B) Schematic of TIAR-2 (Q9U2F5) PrLD with lines indicating mutated serine residues. Red lines represent 2S mutations, black 8S mutations and grey 10S. Mutations in shorter constructs are contained in the larger variants.

C) Quantification of the effects of TIAR-2 serine variants on axon regrowth using single-copy expression transgenes in a *tiar-2(0)* background, shown as a box and whisker plot. Number indicates animals analyzed. One-way ANOVA with Tukey's post-hoc test; $*P < 0.05$; $**P < 0.01$, ns not significant.

D) Graph shows quantification of PLM axons containing granules as %. Number indicates neurons scored. Fisher's exact test; $***P < 0.001$.

E) Representative spinning disc confocal image and kymograph of GFP-TIAR-2(2SE) [*juEx7990*] in a PLM axon. Kymograph was created using 17 s of spinning disc imaging and 10 μm of axon.

F) Quantification of circularity of GFP-TIAR-2[*juSi542*] and GFP-TIAR-2(2SE) [*juEx7990/7991*] granules, shown as a dot plot. Number is granules analyzed, from 7 animals. Mann-Whitney U Test, $***P < 0.001$.

G) Quantification of fission and fusion events of GFP-TIAR-2[*juSi542*] and GFP-TIAR-2(2SE)[*juEx7990/7991*] granules, shown as a box and whisker plot. Number indicates animals analyzed.

H) Left: Representative confocal images of GFP-TIAR-2(2SA)[*juSi374*] and (2SE)[*juSi379*] 15 min post-axotomy. Fire' Lookup table used for visualization of intensity changes. Scale 2 μm. Arrow marks the site of axon injury. Right: Quantification of GFP-TIAR-2(2SE) and (2SA) granules 15min following axotomy, shown as a box and whisker plot. Number indicates animals analyzed. Unpaired Student's T-test; $*P < 0.05$.

KEY RESOURCES TABLE

REAGENT or RESOURCE	SOURCE	IDENTIFIER
Antibodies		
Mouse monoclonal phospho-tyrosine antibody (PY99)	Santa Cruz Biotech	sc-7020
Rabbit polyclonal GFP antibody	Abcam	ab290
Mouse monoclonal phospho-serine antibody (16B4)	Santa Cruz Biotech	sc-81515
Bacterial and Virus Strains		
Rosetta DE3 Competent Cells	Sigma Aldrich	Cat#70954
E.coli: OP50	Caenorhabditis Genetics Center	RRID: WB-STRAIN:OP50
Chemicals, Peptides, and Recombinant Proteins		
Protein: GFP-TIAR-2	This study	N/A
Protein: TIAR-2	This study	N/A
Protein: Cas9-NLS	QB3 MacroLab, UC Berkeley	N/A
Critical Commercial Assays		
µMacs GFP Isolation Kit	Miltenyi Biotech	Cat# 130–091-125
Experimental Models: Organisms/Strains		
C. elegans strain: *zdIs5[Pmec-4-GFP] I*	This study	CZ22812
C. elegans strain: *zdIs5[Pmec-4-GFP] I; tiar-2(ju1401) II*	This study	CZ24738
C. elegans strain: *zdIs5[Pmec-4-GFP] I; tiar-2(tm2923) II*	This study	CZ22811
C. elegans strain: *zdIs5[Pmec-4-GFP] I; tiar-2(tm2923) II juSi324[Pmyo-3-GFP-TIAR-2] IV*	This study	CZ23840
C. elegans strain: *zdIs5[Pmec-4-GFP] I; tiar-2(tm2923) II; juSi306[Pmec-4-GFP-TIAR-2) IV*	This study	CZ23837
C. elegans strain: *zdIs5[Pmec-4-GFP] I; tiar-2(tm2923) II; juSi340[Pmec-4-GFP-TIA1] IV*	This study	CZ25021
C. elegans strain: *juEx7414[Pmec-4-mKate2, Ptiar-2-GFP-TIAR-2, Pmyo-2-mCherry]*	This study	CZ24902
C. elegans strain: *juEx7416[Pmec-4-mKate2, Ptiar-2-GFP-TIAR-2, Pmyo-2-mCherry]*	This study	CZ24904
C. elegans strain: *tiar-2(tm2923) II; juSi306[Pmec-4-GFP-TIAR-2)*	This study	CZ23834
C. elegans strain: *juSi306[Pmec-4-GFP-TIAR-2) IV*	This study	CZ23833
C. elegans strain: *tiar-2(tm2923) II; juIs542[Pmec-4-GFP-TIAR-2]*	This study	CZ24667
C. elegans strain: *zdIs5[Pmec4-GFP] I; tiar-2(tm2923) II; juIs542[Pmec-4-GFP-TIAR-2]*	This study	CZ26542
C. elegans strain: *juEx7943[Pmec-4-GFP-TIAR-1, Pmyo-2-mCherry]*	This study	CZ26842
C. elegans strain: *juEx7944[Pmec-4-GFP-TIAR-1, Pmyo-2-mCherry]*	This study	CZ26843
C. elegans strain: *juEx7945[Pmec-4-GFP-TIAR-1, Pmyo-2-mCherry]*	This study	CZ26844
C. elegans strain: *zdIs5[Pmec4-GFP] I*	(Chen et al., 2011)	CZ10175
C. elegans strain: *zdIs5[Pmec4-GFP] I; tiar-1(tm361) II*	(Kim et al., 2018)	CZ19838

REAGENT or RESOURCE	SOURCE	IDENTIFIER
C. elegans strain: *zdIs5[Pmec4-GFP] I; tiar-2(tm2923) II; juSi373[Pmec-4-GFP-TIAR-1] IV*	This study	CZ26845
C. elegans strain: *juEx7907[Pmec-4-mKate2-TIAR-2, Pmyo-2-mCherry]*	This study	CZ26573
C. elegans strain: *juEx7908[Pmec-4-mKate2-TIAR-2, Pmyo-2-mCherry]*	This study	CZ26574
C. elegans strain: *juEx7909[Pmec-4-mKate2-TIAR-2, Pmyo-2-mCherry]*	This study	CZ26575
C. elegans strain: *tiar-1(tn1545) II; juEx7940[Pmec-4-mKate2, Pmyo-2-mCherry]*	This study (Huelgas-Morales et al., 2016)	CZ26839
C. elegans strain: *tiar-1(tn1545) II; juEx7941[Pmec-4-mKate2, Pmyo-2-mCherry]*	This study (Huelgas-Morales et al., 2016)	CZ26840
C. elegans strain: *tiar-1(tn1545) II; juEx7942[Pmec-4-mKate2, Pmyo-2-mCherry]*	This study(Huelgas-Morales et al., 2016)	CZ26841
C. elegans strain: *juIs542[Pmec-4-GFP-TIAR-2]; juEx8007[Pmec-4-mKate2-TIAR-2, Pmyo-2-mCherry]*	This study	CZ27307
C. elegans strain: *juIs542[Pmec-4-GFP-TIAR-2]; juEx8008[Pmec-4-mKate2-TIAR-2, Pmyo-2-mCherry]*	This study	CZ27308
C. elegans strain: *tiar-2(tm2923) II; gtbp-1(ax2053) IV; juEx8007[Pmec-4-mKate2-TIAR-2, Pmyo-2-mCherry]*	This study (Paix et al., 2014)	CZ27155
C. elegans strain: *tiar-2(tm2923) II; gtbp-1(ax2053) IV; juEx8008[Pmec-4-mKate2-TIAR-2, Pmyo-2-mCherry]*	This study (Paix et al., 2014)	CZ27156
C. elegans strain: *jsIs821[Pmec-7-GFP-RAB-3], jsIs1073[Pmec-7-tagRFP-Cox8A]*	This study (Zheng et al., 2014)	CZ27105
C. elegans strain: *tiar-2(tm2923) II; gtbp-1(ax2068) IV; juIs542[Pmec-4-GFP-TIAR-2]*	This study	CZ27356
C. elegans strain: *juIs542[Pmec-4-GFP-TIAR-2], juEx7947[Pmec-4-mKate2-AIN-1, Pmyo-2-mCherry]*	This study	CZ26908
C. elegans strain: *juIs542[Pmec-4-GFP-TIAR-2], juEx7948[Pmec-4-mKate2-AIN-1, Pmyo-2-mCherry]*	This study	CZ26909
C. elegans strain: *jsIs1263[Pmec-7-tagRFP-RAB-3], juIs542[Pmec-4-GFP-TIAR-2]*	This study (Zheng et al., 2014)	CZ26906
C. elegans strain: *jsIs1075[Pmec-7-tagRFP-ELKS], juIs542[Pmec-4-GFP-TIAR-2]*	This study (Zheng et al., 2014)	CZ26981
C. elegans strain: *jsIs1073[Pmec-7-tagRFP-Cox8A], juIs542[Pmec-4-GFP-TIAR-2]*	This study (Zheng et al., 2014)	CZ27022
C. elegans strain: *juSi386[Pmec-4-GFP-STAU-1] IV; juIs542[Pmec-4-GFP-TIAR-2]*	This study	CZ27104
C. elegans strain: *bpIs37[Pdcp-1-DCP-1-dsRed, rol-6(+)], juIs542[Pmec-4-GFP-TIAR-2]*	This study (Sun et al., 2011)	CZ26962
C. elegans strain: *stau-1(ma327) X; tiar-2(tm2923) II; juIs542[Pmec-4-GFP-TIAR-2]*	This study	CZ27357
C. elegans strain: *juSi10[Pmec-4-GFP]*	This study	CZ11094
C. elegans strain: *zdIs5[Pmec4-GFP] I; tiar-2(tm2923) II; juSi307[Pmec-4-GFP-TIAR-2(ΔRRM1–3)]*	This study	CZ23876
C. elegans strain: *zdIs5[Pmec4-GFP] I; tiar-2(tm2923) II; juSi332[Pmec-4-GFP-TIAR-2(ΔPrLD)]*	This study	CZ25247
C. elegans strain: *zdIs5[Pmec4-GFP] I; tiar-2(tm2923) II; juSi330[Pmec-4-GFP-TIAR-2(ΔGlyRich)]*	This study	CZ24615
C. elegans strain: *tiar-2(tm2923) II; juEx7857[Pmec-4-GFP-TIAR-2, Pmyo-2-mCherry]*	This study	CZ26356
C. elegans strain: *tiar-2(tm2923) II; juEx7858[Pmec-4-GFP-TIAR-2, Pmyo-2-mCherry]*	This study	CZ26357

REAGENT or RESOURCE	SOURCE	IDENTIFIER
C. elegans strain: *tiar-2(tm2923) II; juEx7859[Pmec-4-GFP-TIAR-2, Pmyo-2-mCherry]*	This study	CZ26358
C. elegans strain: *tiar-2(tm2923) II; juEx7860[Pmec-4-GFP-TIAR-2(ΔPrLD), Pmyo-2-mCherry]*	This study	CZ26359
C. elegans strain: *tiar-2(tm2923) II; juEx7861[Pmec-4-GFP-TIAR-2(ΔPrLD), Pmyo-2-mCherry]*	This study	CZ26360
C. elegans strain: *tiar-2(tm2923) II; juEx7864[Pmec-4-GFP-TIAR-2(ΔRRM1–3), Pmyo-2-mCherry]*	This study	CZ26363
C. elegans strain: *tiar-2(tm2923) II; juEx7865[Pmec-4-GFP-TIAR-2(ΔRRM1–3), Pmyo-2-mCherry]*	This study	CZ26364
C. elegans strain: *tiar-2(tm2923) II; juEx7862[Pmec-4-GFP-TIAR-2(ΔGlyRich), Pmyo-2-mCherry]*	This study	CZ26361
C. elegans strain: *tiar-2(tm2923) II; juEx7863[Pmec-4-GFP-TIAR-2(ΔGlyRich), Pmyo-2-mCherry]*	This study	CZ26362
C. elegans strain: *juIs24[Pvab-1-GFP-VAB-1]*	(George et al., 1998)	CZ723
C. elegans strain: *zdIs5[Pmec4-GFP] I; tiar-2(tm2923) II; juSi383[Pmec-4-GFP-TIAR-2(9YG)] IV*	This study	CZ27004
C. elegans strain: *zdIs5[Pmec4-GFP] I; tiar-2(tm2923) II; juSi380[Pmec-4-GFP-TIAR-2(6YG)] IV*	This study	CZ26975
C. elegans strain: *zdIs5[Pmec4-GFP] I; tiar-2(tm2923) II; juSi385[Pmec-4-GFP-TIAR-2(3YG)] IV*	This study	CZ27006
C. elegans strain: *zdIs5[Pmec4-GFP] I; tiar-2(tm2923) II; juSi384[Pmec-4-GFP-TIAR-2(7GY)] IV*	This study	CZ27005
C. elegans strain: *zdIs5[Pmec4-GFP] I; tiar-2(tm2923) II; juSi382[Pmec-4-GFP-TIAR-2(5GY)] IV*	This study	CZ26977
C. elegans strain: *zdIs5[Pmec4-GFP] I; tiar-2(tm2923) II; juSi381[Pmec-4-GFP-TIAR-2(3GY)] IV*	This study	CZ26976
C. elegans strain: *tiar-2(tm2923) II; juEx7968[Pmec-4-GFP-TIAR-2(9YG), Pmyo-2-mCherry]*	This study	CZ27064
C. elegans strain: *tiar-2(tm2923) II; juEx7969[Pmec-4-GFP-TIAR-2(9YG), Pmyo-2-mCherry]*	This study	CZ27065
C. elegans strain: *tiar-2(tm2923) II; juEx7978[Pmec-4-GFP-TIAR-2(6YG), Pmyo-2-mCherry]*	This study	CZ27074
C. elegans strain: *tiar-2(tm2923) II; juEx7979[Pmec-4-GFP-TIAR-2(6YG), Pmyo-2-mCherry]*	This study	CZ27075
C. elegans strain: *tiar-2(tm2923) II; juEx7976[Pmec-4-GFP-TIAR-2(3YG), Pmyo-2-mCherry]*	This study	CZ27072
C. elegans strain: *tiar-2(tm2923) II; juEx7977[Pmec-4-GFP-TIAR-2(3YG), Pmyo-2-mCherry]*	This study	CZ27073
C. elegans strain: *tiar-2(tm2923) II; juEx7970[Pmec-4-GFP-TIAR-2(7GY), Pmyo-2-mCherry]*	This study	CZ27066
C. elegans strain: *tiar-2(tm2923) II; juEx7971[Pmec-4-GFP-TIAR-2(7GY), Pmyo-2-mCherry]*	This study	CZ27067
C. elegans strain: *tiar-2(tm2923) II; juEx7982[Pmec-4-GFP-TIAR-2(5GY), Pmyo-2-mCherry]*	This study	CZ27078
C. elegans strain: *tiar-2(tm2923) II; juEx7983[Pmec-4-GFP-TIAR-2(5GY), Pmyo-2-mCherry]*	This study	CZ27079
C. elegans strain: *tiar-2(tm2923) II; juEx7980[Pmec-4-GFP-TIAR-2(3GY), Pmyo-2-mCherry]*	This study	CZ27076
C. elegans strain: *tiar-2(tm2923) II; juEx7981[Pmec-4-GFP-TIAR-2(3GY), Pmyo-2-mCherry]*	This study	CZ27077

REAGENT or RESOURCE	SOURCE	IDENTIFIER
C. elegans strain: *zdIs5[Pmec4-GFP] I; tiar-2(tm2923) II; juSi376[Pmec-4-GFP-TIAR-2(10SA)] IV*	This study	CZ26954
C. elegans strain: *zdIs5[Pmec4-GFP] I; tiar-2(tm2923) II; juSi377[Pmec-4-GFP-TIAR-2(8SA)] IV*	This study	CZ26955
C. elegans strain: *zdIs5[Pmec4-GFP] I; tiar-2(tm2923) II; juSi374[Pmec-4-GFP-TIAR-2(2SA)] IV*	This study	CZ26893
C. elegans strain: *zdIs5[Pmec4-GFP] I; tiar-2(tm2923) II; juSi375[Pmec-4-GFP-TIAR-2(10SE)] IV*	This study	CZ26953
C. elegans strain: *zdIs5[Pmec4-GFP] I; tiar-2(tm2923) II; juSi378[Pmec-4-GFP-TIAR-2(8SE)] IV*	This study	CZ26956
C. elegans strain: *zdIs5[Pmec4-GFP] I; tiar-2(tm2923) II; juSi379[Pmec-4-GFP-TIAR-2(2SE)] IV*	This study	CZ26957
C. elegans strain: *tiar-2(tm2923) II; juEx7974[Pmec-4-GFP-TIAR-2(10SA), Pmyo-2-mCherry]*	This study	CZ27070
C. elegans strain: *tiar-2(tm2923) II; juEx7975[Pmec-4-GFP-TIAR-2(10SA), Pmyo-2-mCherry]*	This study	CZ27071
C. elegans strain: *tiar-2(tm2923) II; juEx7984[Pmec-4-GFP-TIAR-2(8SA), Pmyo-2-mCherry]*	This study	CZ27080
C. elegans strain: *tiar-2(tm2923) II; juEx7985[Pmec-4-GFP-TIAR-2(8SA), Pmyo-2-mCherry]*	This study	CZ27081
C. elegans strain: *tiar-2(tm2923) II; juEx7986[Pmec-4-GFP-TIAR-2(2SA), Pmyo-2-mCherry]*	This study	CZ27086
C. elegans strain: *tiar-2(tm2923) II; juEx7987[Pmec-4-GFP-TIAR-2(2SA), Pmyo-2-mCherry]*	This study	CZ27087
C. elegans strain: *tiar-2(tm2923) II; juEx7972[Pmec-4-GFP-TIAR-2(10SE), Pmyo-2-mCherry]*	This study	CZ27068
C. elegans strain: *tiar-2(tm2923) II; juEx7973[Pmec-4-GFP-TIAR-2(10SE), Pmyo-2-mCherry]*	This study	CZ27069
C. elegans strain: *tiar-2(tm2923) II; juEx7988[Pmec-4-GFP-TIAR-2(8SE), Pmyo-2-mCherry]*	This study	CZ27088
C. elegans strain: *tiar-2(tm2923) II; juEx7989[Pmec-4-GFP-TIAR-2(8SE), Pmyo-2-mCherry]*	This study	CZ27089
C. elegans strain: *tiar-2(tm2923) II; juEx7990[Pmec-4-GFP-TIAR-2(2SE), Pmyo-2-mCherry]*	This study	CZ27090
C. elegans strain: *tiar-2(tm2923) II; juEx7991[Pmec-4-GFP-TIAR-2(2SE), Pmyo-2-mCherry]*	This study	CZ27091
C. elegans strain: *muIs32[Pmec-7-GFP] II*	(Chen et al., 2011)	CZ10969
C. elegans strain: *stau-1 (tm2266) X; muIs32[Pmec-7-GFP] II*	(Kim et al., 2018)	CZ16956
C. elegans strain: *rskn-1 (tm4834) I; muIs32[Pmec-7-GFP] II*	(Hubert et al., 2014)	CZ17111
C. elegans strain: *zdIs5[Pmec4-GFP] I; rack-1(tm2262) IV*	(Chen et al., 2011)	CZ11086
C. elegans strain: *muIs32[Pmec-7-GFP] II, exc-7(rh252)II*	(Chen et al., 2011)	CZ9296
C. elegans strain: *zdIs5[Pmec4-GFP] I; gtbp-1(ax2068) IV*	(Kim et al., 2018)	CZ23558
C. elegans strain: *zdIs5[Pmec4-GFP] I; tiar-2(tm2923) II*	(Kim et al., 2018)	CZ19839
Oligonucleotides		
Alt-R CRISPR-Cas9 tracrRNA	Integrated DNA Technologies	Cat#1072532
Alt-R CRISPR-Cas9 crRNA to make tiar-2(ju1401) deletion: cttcgttctacacgggaggt	Integrated DNA Technologies	N/A

REAGENT or RESOURCE	SOURCE	IDENTIFIER
Alt-R CRISPR-Cas9 crRNA to make tiar-2(ju1401) deletion: gcattcgagccccgcgagcc	Integrated DNA Technologies	N/A
qRT-PCR Primer *tiar-2 FOR:*GACGGCTTCAATCCCCGTGT	Integrated DNA Technologies	N/A
qRT-PCR Primer *tiar-2 REV:*CCACGAAAGCGTACGGATCG	Integrated DNA Technologies	N/A
qRT-PCR Primer *rps-25 FOR:*CTCTACAAGGAGGTCATCACC	Integrated DNA Technologies	N/A
qRT-PCR Primer *rps-25 REV:*GACCTGTCCGTGATGATGAACG	Integrated DNA Technologies	N/A
Recombinant DNA		
Plasmid: *Peft-3:Cas9 + cxTi10882* sgRNA	This study	pCZGY2750
Plasmid: *Pmec-4-GFP-TIAR-2* for *juSi306* CRISPR/Cas9 knock-in	This study	pCZGY3294
Plasmid: *Pmyo-3-GFP-TIAR-2* for *juSi324* CRISPR/Cas9 knock-in	This study	pCZGY3295
Plasmid: *Pmec-4-GFP-TIA1* for *juSi340* CRISPR/Cas9 knock-in	This study	pCZGY3296
Plasmid: *Pmec-4-mKate2*	This study	pCZGY2948
Plasmid: *Ptiar-2-GFP-TIAR-2*	This study	pCZGY3301
Plasmid: *Pmec-4-GFP-TIAR-2*	This study	pCZGY2701
Plasmid: *Pmec-4-GFP-TIAR-1*	This study	pCZGY3404
Plasmid: *Pmec-4-GFP-TIAR-1* for *juSi373* CRISPR/Cas9 knock-in	This study	pCZGY3405
Plasmid: *Pmec-4-mKate2-TIAR-2*	This study	pCZGY3338
Plasmid: *Pmec-4-mKate2-AIN-1*	This study	pCZGY3403
Plasmid: *Pmec-4-mKate2-STAU-1* for *juSi386* CRISPR/Cas9 knock-in	This study	pCZGY3402
Plasmid: *Pet15-TIAR-2*	This study	pCZGY3406
Plasmid: *Pet15-GFP-TIAR-2*	This study	pCZGY3407
Plasmid: *Pmec-4-GFP-TIAR-2 (ΔRRM1–3)* for *juSi307* CRISPR/Cas9 knock-in	This study	pCZGY3297
Plasmid: *Pmec-4-GFP-TIAR-2 (ΔPrLD)* for *juSi332* CRISPR/Cas9 knock-in	This study	pCZGY3298
Plasmid: *Pmec-4-GFP-TIAR-2 (ΔGlyRich)* for *juSi330* CRISPR/Cas9 knock-in	This study	pCZGY3299
Plasmid: *Pmec-4-GFP-TIAR-2 (ΔRRM1–3)*	This study	pCZGY3297
Plasmid: *Pmec-4-GFP-TIAR-2 (ΔPrLD)*	This study	pCZGY3298
Plasmid: *Pmec-4-GFP-TIAR-2 (ΔGlyRich)*	This study	pCZGY3299
Plasmid: *Pmec-4-GFP-TIAR-2 (9YG)* for *juSi383* CRISPR/Cas9 knock-in	This study	pCZGY3391
Plasmid: *Pmec-4-GFP-TIAR-2 (6YG)* for *juSi380* CRISPR/Cas9 knock-in	This study	pCZGY3393
Plasmid: *Pmec-4-GFP-TIAR-2 (3YG)* for *juSi385* CRISPR/Cas9 knock-in	This study	pCZGY3395
Plasmid: *Pmec-4-GFP-TIAR-2 (7GY)* for *juSi384* CRISPR/Cas9 knock-in	This study	pCZGY3397
Plasmid: *Pmec-4-GFP-TIAR-2 (5GY)* for *juSi382* CRISPR/Cas9 knock-in	This study	pCZGY3399
Plasmid: *Pmec-4-GFP-TIAR-2 (3GY)* for *juSi381* CRISPR/Cas9 knock-in	This study	pCZGY3401
Plasmid: *Pmec-4-GFP-TIAR-2 (9YG)*	This study	pCZGY3390
Plasmid: *Pmec-4-GFP-TIAR-2 (6YG)*	This study	pCZGY3392
Plasmid: *Pmec-4-GFP-TIAR-2 (3YG)*	This study	pCZGY3394
Plasmid: *Pmec-4-GFP-TIAR-2 (7GY)*	This study	pCZGY3396
Plasmid: *Pmec-4-GFP-TIAR-2 (5GY)*	This study	pCZGY3398
Plasmid: *Pmec-4-GFP-TIAR-2 (3GY)*	This study	pCZGY3400

REAGENT or RESOURCE	SOURCE	IDENTIFIER
Plasmid: *Pmec-4-GFP-TIAR-2 (10SA)* for *juSi376* CRISPR/Cas9 knock-in	This study	pCZGY3379
Plasmid: *Pmec-4-GFP-TIAR-2 (8SA)* for *juSi377* CRISPR/Cas9 knock-in	This study	pCZGY3381
Plasmid: *Pmec-4-GFP-TIAR-2 (2SA)* for *juSi374* CRISPR/Cas9 knock-in	This study	pCZGY3383
Plasmid: *Pmec-4-GFP-TIAR-2 (10SE)* for *juSi375* CRISPR/Cas9 knock-in	This study	pCZGY3385
Plasmid: *Pmec-4-GFP-TIAR-2 (8SE)* for *juSi378* CRISPR/Cas9 knock-in	This study	pCZGY3387
Plasmid: *Pmec-4-GFP-TIAR-2 (2SE)* for *juSi379* CRISPR/Cas9 knock-in	This study	pCZGY3389
Plasmid: *Pmec-4-GFP-TIAR-2 (10SA)*	This study	pCZGY3378
Plasmid: *Pmec-4-GFP-TIAR-2 (8SA)*	This study	pCZGY3380
Plasmid: *Pmec-4-GFP-TIAR-2 (2SA)*	This study	pCZGY3382
Plasmid: *Pmec-4-GFP-TIAR-2 (10SE)*	This study	pCZGY3384
Plasmid: *Pmec-4-GFP-TIAR-2 (8SE)*	This study	pCZGY3386
Plasmid: *Pmec-4-GFP-TIAR-2 (2SE)*	This study	pCZGY3388
Plasmid: *Pmyo-2-mCherry*	(Frokjaer-Jensen et al., 2008)	pCJF90
Software and Algorithms		
Graphpad Prism 5.0	Graphpad Software,Inc.	RRID:SCR_002798
FIJI	ImageJ; NationalInstitutes of Health	RRID:SCR_002285
ZEN	Zeiss	https://www.zeiss.com/microscopy/us/downloads/zen.html
Prion-like Amino Acid Composition	Lancaster et al. 2014	http://plaac.wi.mit.edu/
NetPhos3.1	DTU Bioinformatics	http://www.cbs.dtu.dk/services/NetPhos/